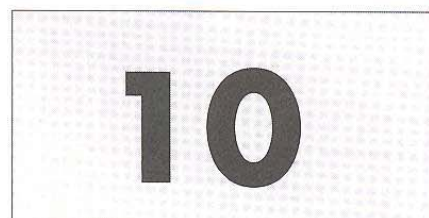# Self-assembly strategy of nanomanufacturing of hybrid devices

10

S. Hong, Y.-K. Kwon, J.S. Ha, N.-K. Lee, B. Kim, and M. Sung

10.1 Introduction

As the conventional device industry reaches its technological and economical limits, extensive efforts have been directed to explore new device architectures utilizing nanomaterials such as nanoparticles, organic molecules, carbon nanotubes (CNTs), and nanowires (NWs). These new devices are often called "hybrid devices" because they are comprised of new nanomaterials as well as conventional electronic elements. Examples include carbon-nanotube-based circuits, molecular electronics, etc. However, a major stumbling block holding back their practical applications can be a lack of a mass-production method for such devices. Since most new nanostructures are first synthesized in a solution or powder form, one has to pick up and assemble millions of individual nanostructures onto solid substrate to build integrated devices, which can be an extremely time-consuming task. On the other hand, biological systems have adapted self-assembly strategy to build macroscale systems from nanoscale molecular structures for billions of years. This chapter will discuss how the self-assembly strategy can be applied for nanomanufacturing of hybrid nanodevices.

10.2 Direct patterning of nanostructures

10.2.1 Dip-pen nanolithography

10.2.1.1 *Basic concept of dip-pen nanolithography*

Dip-pen nanolithography (DPN) is a novel lithography technique that was first developed by Mirkin's group at Northwestern University in 1998 (Piner *et al.* 1999). It is based on an atomic force microscope (AFM) and uses an AFM tip as a nanoscale pen, molecular substances as an ink, and solid substrates as a paper.

The DPN method has several advantages over other lithography techniques such as high resolution and registration, extremely versatile chemical and material flexibility, etc. In addition, there is no need to pre-modify the surface.

AFM Tip

Molecular Diffusion

Tip Movement

Water Condensation

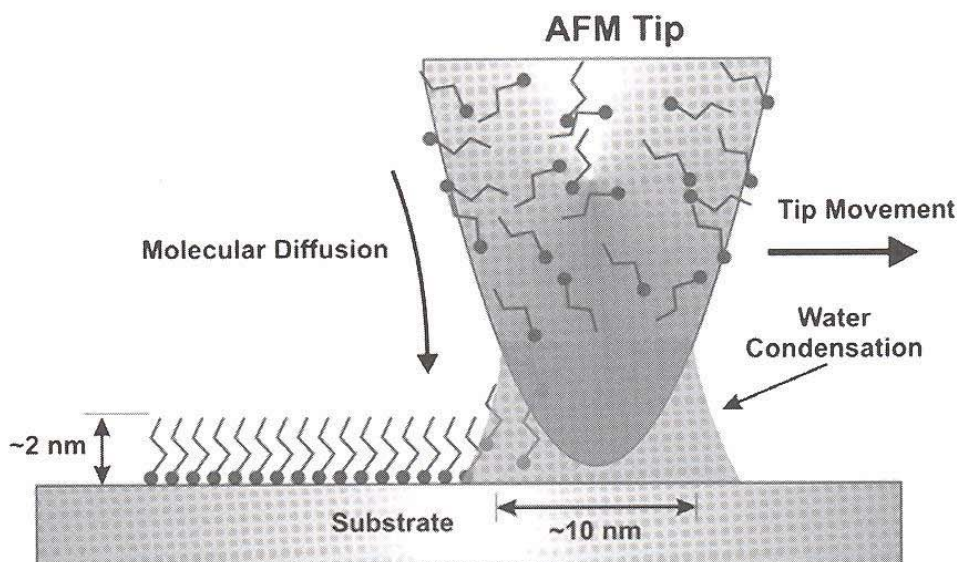~2 nm

Substrate   ~10 nm

Fig. 10.1 Basic mechanism of DPN.

These merits make DPN a unique and highly desirable tool for depositing biological and other soft materials on various surfaces.

Figure 10.1 shows the basic mechanism of DPN as well as transport scheme of a molecular "ink" from the tip to a substrate. When the molecule-coated tip is held in contact with the substrate, the molecules spread out by diffusion onto the substrate. Various-shape patterns are generated on the substrate by scanning the tip. Under ambient conditions, a water condensation forms between the AFM tip and the substrate. The size of the condensation is controlled by the relative humidity and affects the ink molecule transport rate, the effective tip–substrate contact area, and resolution.

10.2.1.2 *Self-assembled monolayer molecules*

Various molecules can be used as DPN ink. Figure 10.2 shows typical organic molecules forming self-assembled monolayers (SAMs) on substrates. Such molecules are composed of a chemisorbing group, spacer, and end-groups. If these molecules are placed onto the substrate, they are chemisorbed onto the substrate and generate a well-ordered stable crystalline monolayer film with a few nanometer thickness. Specific chemisorbing groups can be chosen depending on the substrate. By depositing these molecules onto the substrate, one can completely change the chemical properties of the surface to that of the end-group.

10.2.1.3 *Diffusion theory*

When an AFM tip coated with ink molecules is held at a specific position on the solid substrate, the ink molecules diffuse out onto the substrate and form dot patterns of various sizes with respect to tip-dwelling time (Jang *et al.* 2001; Sheehan *et al.* 2002). To explain this phenomenon, the "double-molecular-layer" (DML) model was proposed, as shown in Figure 10.3 (Cho *et al.* 2006).

Since the DPN process usually utilizes a molecular species that has a higher melting point than room temperature and the tip is dried by N_2 blowing, most of the molecular layer on the tip can be assumed to
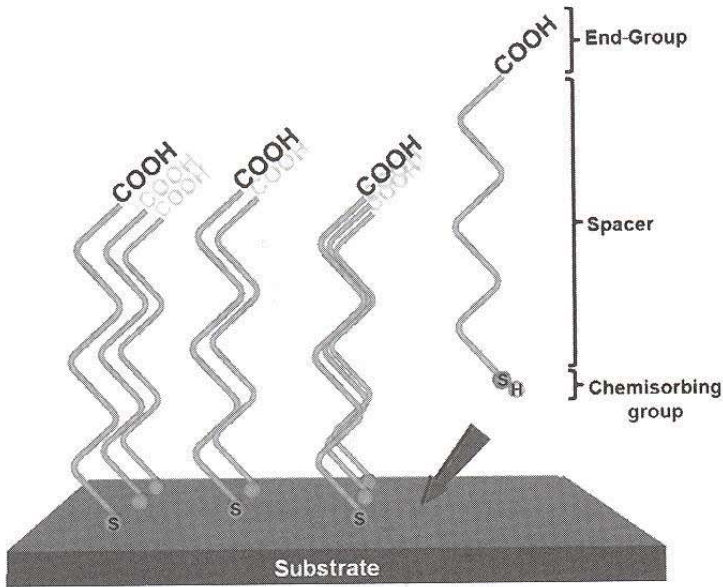
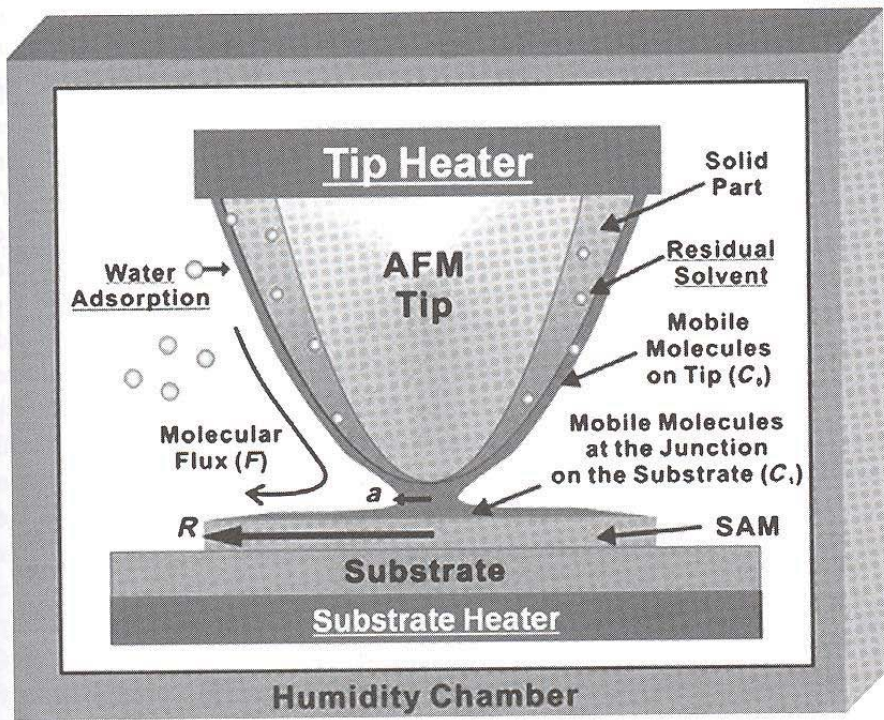**Fig. 10.2** Self-assembled monolayer molecules.

Fig. 10.3 Basic concepts of the DML model. Thermal energy, residual solvent and adsorbed water molecules affect molecular diffusion.

remain solid during the DPN process under ambient conditions. On the other hand, molecules on the surface of the molecular coating are likely to be much more mobile than those inside the molecular layer (Dash 1989). For this reason, the DML model assumes that the molecular ink forms a DML structure comprised of a bulk solid part and a thin mobile surface layer on the tip. The "solid part" continuously provides molecules to the mobile surface layer. Thus, the solid part plays the role of an ink reservoir by stabilizing the deposition rate in the DPN process. The DML

model suggests that the transport rate of molecules in DPN is mainly determined by the mobility and the number density of the mobile surface molecules.

The mobility of the surface molecules can be affected by the following factors; thermal energy, residual solvent and adsorbed water. Thermal energy increases the molecular diffusion constant and enhances the molecular flow. When the temperature goes up near the melting point, the diffusion constant of the surface molecules increases rapidly even for a small temperature variation. Therefore, if the melting point of the molecular ink becomes close to ambient, the deposition rate becomes strongly dependent on temperature. When the tip surface is coated with ink molecules, some residual solvent molecules should remain in the molecular coating, and they can enhance the surface molecular diffusion. When the DPN process is performed under ambient conditions, water from the air can be adsorbed onto the tip and substrate and then affect the mobility of the transporting molecules. In the case of hydrophilic molecular inks, the adsorbed water should improve the mobility.

The diffusion equation of DPN pattern generation can be solved using the DML model. The behavior of the ink molecules can be defined in the following four regions; tip region, nanoscale junction region, SAM region, and bare-substrate region.

In the AFM tip region, the surface density of mobile molecules on the tip C_0 is assumed constant because the solid part of the molecular ink works as an ink reservoir. In the nanoscale junction region, assuming that the junction has circular cross-section with a radius a and that the net molecular transport is determined by the difference between flux transported toward the surface and that away from the surface, the molecular flux through the nanoscale junction can be described as Flux $= 2\pi a \ (\alpha_0 C_0 - \alpha_1 C_1)$, where α_0 and α_1 are the molecular transport rate coefficients from the tip to the substrate and that from the substrate to the tip, respectively. C_1 is the density of mobile molecules on the substrate at the junction. It should be noted that α_0 and α_1 depend on various factors such as the water meniscus at the junction and attractive forces between the substrate and the molecules. However, when the substrate is covered by molecular layers, the diffusion coefficients are about the same on the tip and substrate, so $\alpha_0 = \alpha_1 \equiv \alpha$ and Flux $= 2\pi a \alpha$ $(C_0 - C_1)$.

On the substrate, the first-deposited molecules are assumed to chemically anchor to the bare substrate and form a uniform SAM. After this initial deposition, the molecules deposited on top of the SAM can diffuse out until they meet bare-substrate regions. In this case, the motion of the molecules on the SAM can be described by the diffusion equation, $\frac{\partial C}{\partial t} = \frac{1}{r} \frac{\partial}{\partial r} \left(r D \frac{\partial C}{\partial r} \right)$, where C and D represent the surface density and diffusion constant of mobile molecules on the substrate, respectively. At the outer boundary of the SAM pattern, the moving boundary condition, $\frac{\partial C}{\partial r} \big|_{r=R} = -C_R \frac{dR}{dt}$, can be used to describe the increase in radius R of the SAM that occurs when molecules reaching the boundary become adhered to the substrate. C_R represents the density of molecules in the SAM. At the nanoscale junction, another boundary condition based on the molecular flux equation, $\frac{\partial C}{\partial r} \big|_{r=a} = \alpha(C_0 - C_1)$, is assumed. This means that molecules transported through the nanoscale junction diffuse onto

the substrate. With proper boundary condition, we can solve for dt/dR as,

$$\frac{dt}{dR} = \frac{1}{D}\left(\frac{C_R}{C_0}\right)\left\{R\ln R + R\left(\frac{D}{a\alpha} - \ln a\right)\right\}, \qquad (10.1)$$

(Crank 1993) Assuming initial deposition of $R \to a$ as $t \to 0$, the solution to eqn (10.1) is

$$t = \frac{1}{4D}\left(\frac{C_R}{C_0}\right)\left\{2R^2\ln(R/a) + (R^2 - a^2)\left(\frac{2D}{a\alpha} - 1\right)\right\}. \qquad (10.2)$$

In the *fast-diffusion limit case* (diffusion rate $\gg$ deposition rate), eqn (10.2) becomes

$$t = \frac{R^2}{4D}\left(\frac{C_R}{C_0}\right)\left(\frac{2D}{a\alpha}\right)\left\{1 + \frac{2D}{a\alpha}\ln(R/a)\right\} \quad (R \gg a, D/a \gg 1). \quad (10.3)$$

From this, we obtain the power-law relation $R \propto t^\nu$, where

$$\nu \cong \frac{1}{2}\left(1 - \frac{a\alpha}{2D}\right). \qquad (10.4)$$

For the *general case* (deposition rate $\sim$ diffusion rate), the general solution eqn (10.2) becomes

$$t \cong \frac{R^2}{4D}\left(\frac{C_R}{C_0}\right)[2\ln(R/a)] \quad (D/a \sim 1, \ln(R/a) \gg [1 - (a^2/R^2)]). \qquad (10.5)$$

Since for $R \gg a$, we have $1 < \ln(R/a) < R/a$, we can write

$$\frac{1}{4D}\left(\frac{C_R}{C_0}\right)2R^2 < t < \frac{1}{4D}\left(\frac{C_R}{C_0}\right)\frac{2R^3}{a}. \qquad (10.6)$$

10.2.1.4 *Application*

The DPN technique can generate patterns with various molecular species such as alkanethiols, biomolecules, salts, and conducting polymers, etc. Chemisorption of a molecular ink onto the substrate forms stable nanostructures, which can subsequently be used as templates to assemble different types of molecules or nanostructures of interest (Demers *et al.* 2001).

Figure 10.4(a) shows the typical procedure of pattern generation using the DPN method. The AFM tip is coated with 16-mercaptohexadecanoic acid (MHA) by dipping into a saturated solution of MHA in acetonitrile for 30 s. The coated tip is blown by compressed N_2 or other gases before being used. MHA patterns are generated by scanning the tip on Au substrate in pre-defined patterns. The patterned Au substrate is dipped into a saturated solution of 1-octadecanethiol (ODT) in acetonitrile for 30 s to form a passivating layer on the Au substrate around the MHA nanostructures. After rinsing with acetonitrile and drying, the samples are dipped into a suspension of the iron-oxide particles (magnetite, Fe_3O_4) for 30 s and then dried under a flow of nitrogen overnight (Fu *et al.* 2001). Figure 10.4(b) shows AFM topography image of iron-oxide dot array generated according to the scheme of Fig. 10.4(a) (Liu *et al.* 2002).
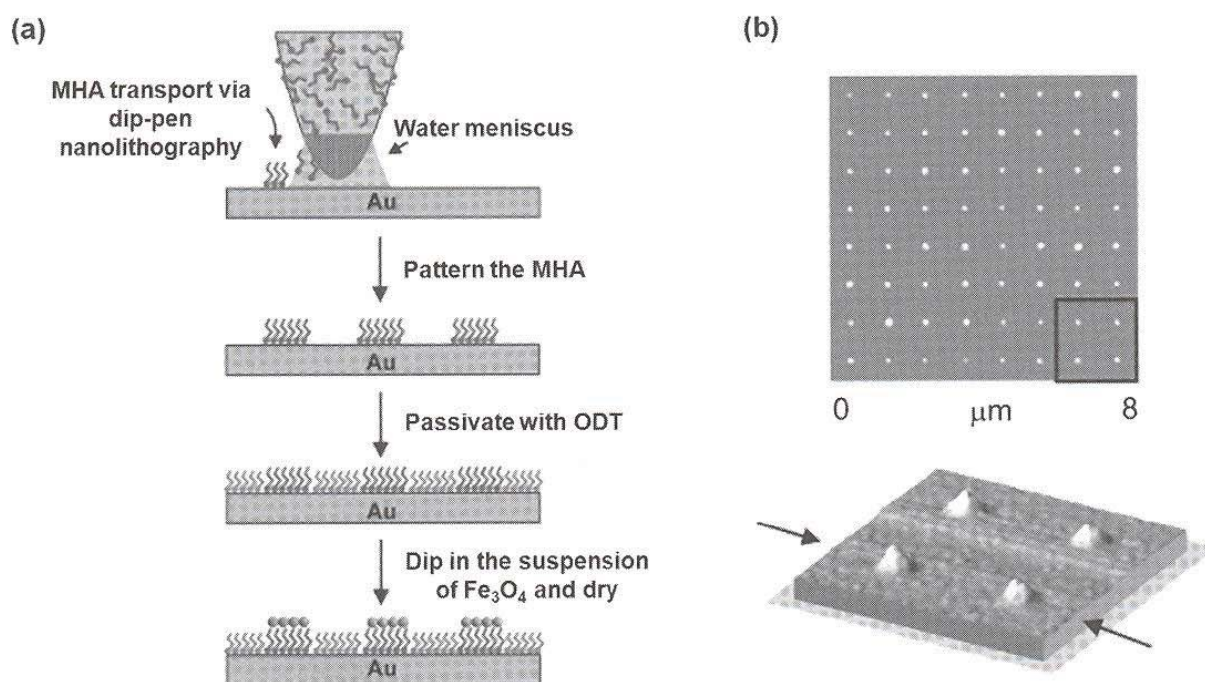
Fig. 10.4 (a) Schematic representation of the procedure used to prepare magnetic nanostructures on a Au substrate. (b) AFM topography image of magnetic structures formed on MHA (from Liu, X., Fu, L., Hong, S., Dravid, V.P. and Mirkin, C.A. (2002) *Adv. Mater.* **14**, 231 ©2002 Copyright Wiley-VCH Verlag GmbH & Co. KGaA., reproduced with permission).

10.2.2   Microcontact printing of nanostructures

Microcontact printing (MCP) is a pattern-transfer technique where the patterned polymer stamp inked with molecules or nanomaterials is physically contacted with substrates and it has the advantage of easy transfer of micropatterns over a large area. This technique was originally adopted to transfer self-assembling molecular monolayers onto Au substrates and then either to etch Au by using such a formed self-assembled monolayer as a passivation layer (Kumar *et al.* 1993; Xia *et al.* 1996) or to fabricate chemical templates (Kumar *et al.* 1994a,b). During the last decade, MCP has been extended to patterning of polymer (Miller *et al.* 2002), metal film (Hur *et al.* 2004, 2005), nanomaterials (Yip *et al.* 2006; Sun *et al.* 2007), and biomaterials including DNA (Bernard *et al.* 2000; Tan *et al.* 2002; Csucs *et al.* 2003). MCP is done at relatively low temperatures, which enables its use on flexible plastic substrates (Yip *et al.* 2006). Owing to the above-mentioned advantages of MCP, there have been extensive efforts to replace the microfabrication process based on the photolithography technique, which is quite complicated and has high costs, with MCP (Xia *et al.* 1998; Love *et al.* 2005; Menard *et al.* 2007). In this section, we discuss several important points that should be understood well for the successful performance of traditional MCP in micropatterning of nanomaterials.

A general schematic of MCP is shown in Fig. 10.5. Since the pattern transfer occurs via physical contact, it is particularly important to have the inked stamp uniformly contacted with substrates and so to use the polymer stamp with elasticity and viscosity. As a stamp material, poly(dimethylsiloxane) (PDMS)

has been most widely used. PDMS is quite rigid to retain the micropatterns of the stamp and is also chemically inert not to be deformed or contaminated by chemicals during the patterning process (Xia *et al.* 1998; Menard *et al.* 2007). High-modulus PDMS or poly(urethaneacrylate) was also actively studied for the patterning of structures smaller than 100 nm (Schmid and Michel 2000) or for the patterning under easy deformation conditions of stamps (Yoo *et al.* 2004; Park *et al.* 2006b).

PDMS has a low surface energy ($\sim$20 N/m) which enables easy transfer of ink materials onto substrate, but it is hydrophobic, which is not good for the uniform inking of polar materials. Materials dispersed in polar solvent forms a circular drop on the PDMS stamp surface with a high contact angle. Polar ink induces dewetting and it is not transferred onto PDMS stamp even under dry condition. Treatment of the hydrophobic stamps with oxygen plasma (Donzel *et al.* 2001; Delamarche *et al.* 2003), UV-ozone (Ouyang *et al.* 2000; Efimenko *et al.* 2002), and acid (Chaudhury *et al.* 1996) resulted in the hydrophilic PDMS stamp. However, such formed hydrophilic stamps recovered the intrinsic hydrophobic properties after a certain period of time (Donzel *et al.* 2001; Delamarche *et al.* 2003; Bodas and Malek 2007). In order to improve it, coating of the PDMS stamp surface via chemical reaction was devised (Donzel *et al.* 2001; Delamarche *et al.* 2003; Bodas and Malek 2007).

Figure 10.6 shows the grafting process of PEG molecules onto a PDMS surface (Park *et al.* 2006b). First, hydroxyl OH groups are formed on the surface via oxidation by O_2 plasma treatment. Then, subsequent treatment with 3-aminopropyltriethoxysilane (APS), bis(sulfosuccinimidyl)-suberate)(BS^3), and amino-terminated polyethylene glycol (NH_2-PEG-NH_2) grafted the PEG molecules into PDMS, which prohibited the recovery of surface hydrophobicity. Instead of PDMS surface modification, use of hydrophilic poly(ether-block-ester) (Trimbach *et al.* 2007) and agarose (Weibel *et al.* 2005) as stamp materials could transfer various kinds of polar inks.

In traditional MCP, ink materials on the relief region of the stamp pattern are transferred onto the substrates as in general printing methods. However, it is also possible to transfer the ink in the recess region of the patterned stamp. In this case, confinement of ink inside the recess area is required and it can be easily done when the interaction between the stamp surface and the ink material is not attractive, which is called "discontinuous dewetting". Figure 10.7 shows one example of patterning via discontinuous dewetting, where the V_2O_5 nanowires in the recess area of the patterned PDMS stamp were transferred onto the substrates (Kim *et al.* 2006). If the hydrophobic stamps were slowly taken out from the V_2O_5 nanowire solution after sufficient dipping time, polar nanowire solution would be stored inside the recess area without inking the relief area of the stamp. Then, evaporation of solvent in air or vacuum can make the concentrated nanowires spontaneously aggregate in the edge of the stamp. Therefore, aggregated nanowire patterns could be transferred via printing of the nanowire inks in the edges. In this way, submicrometer-sized patterns of nanowires could be obtained by using a stamp with micrometer-sized patterns.

On the contrary, use of hydrophilic stamps treated with UV-ozone could produce the transfer of nanowire patterns according to the stamp pattern, as expected. There were also reports on the patterning of Au nanoparticles and
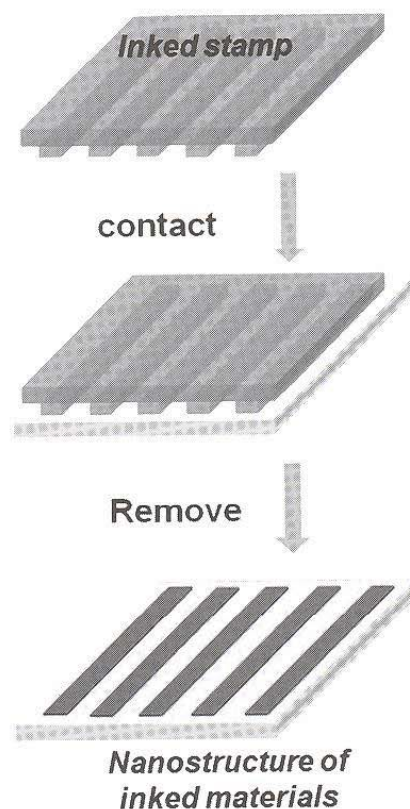

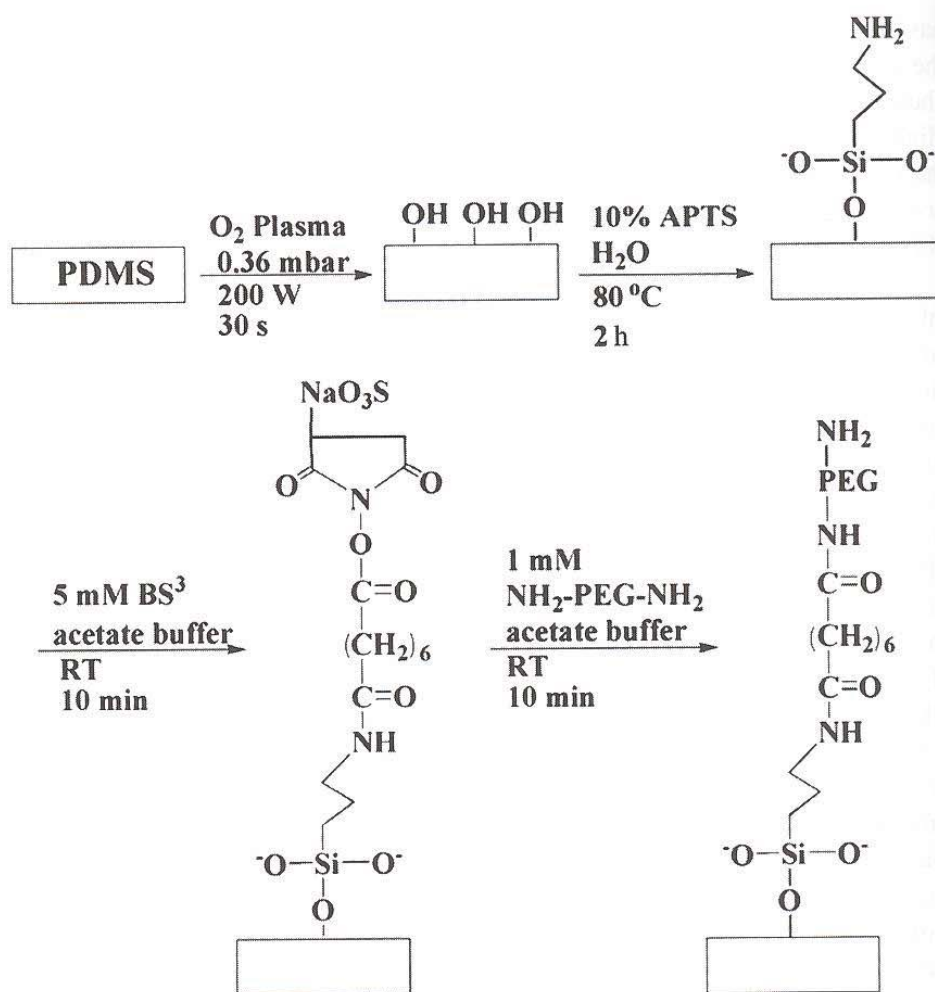**Fig. 10.5** Schematics of microcontact printing.

Fig. 10.6 Preparation of hydrophilic PDMS surface by grafting (from Donzel, C., Geissler, M., Bernard, A., Wolf, H., Michael, B., Hilborn, J. and Delamarche, E. (2001) *Adv. Mater.* **13**, 1164 ©2001 Copyright Wiley-VCH Verlag GmbH & Co. KGaA., reprinted in part with permission).

alkanethiol molecules by use of edge patterns of the stamp (Cherniavskaya 2002).

In general, inking of nanoparticles larger than a few tens of nanometers or the nanowires longer than a few micrometers needs a special recipe, different from that of small charged particles or short-chain molecules. Figure 10.8 introduces the various interesting inking methods. Spin coating can form a uniform film in a short time. Inking of a PDMS stamp with single-wall carbon nanotubes (SWNTs) by spin coating is shown in Fig. 10.8(a) (Meitl *et al.* 2004). Coating of SWNT emulsion could not produce the high-density SWNTs on the stamp due to weak interaction between the PDMS stamp and SWNTs. However, addition of methanol could increase the density of SWNT on the stamp by enhancing the dissipation of more SWNTs via extracting the sodium dodecyl sulfate (SDS) from the SWNT emulsion. Therefore, SWNT patterns could be obtained by direct printing. Interestingly, alignment of SWNTs by centrifugal force during the spin coating was observed.

Via contact of PDMS stamp onto the uniform SWNT film prepared via vacuum filtration of SWNT emulsion dispersed in SDS solution by using an alumina filter, a transparent electrode pattern could be transferred, with a
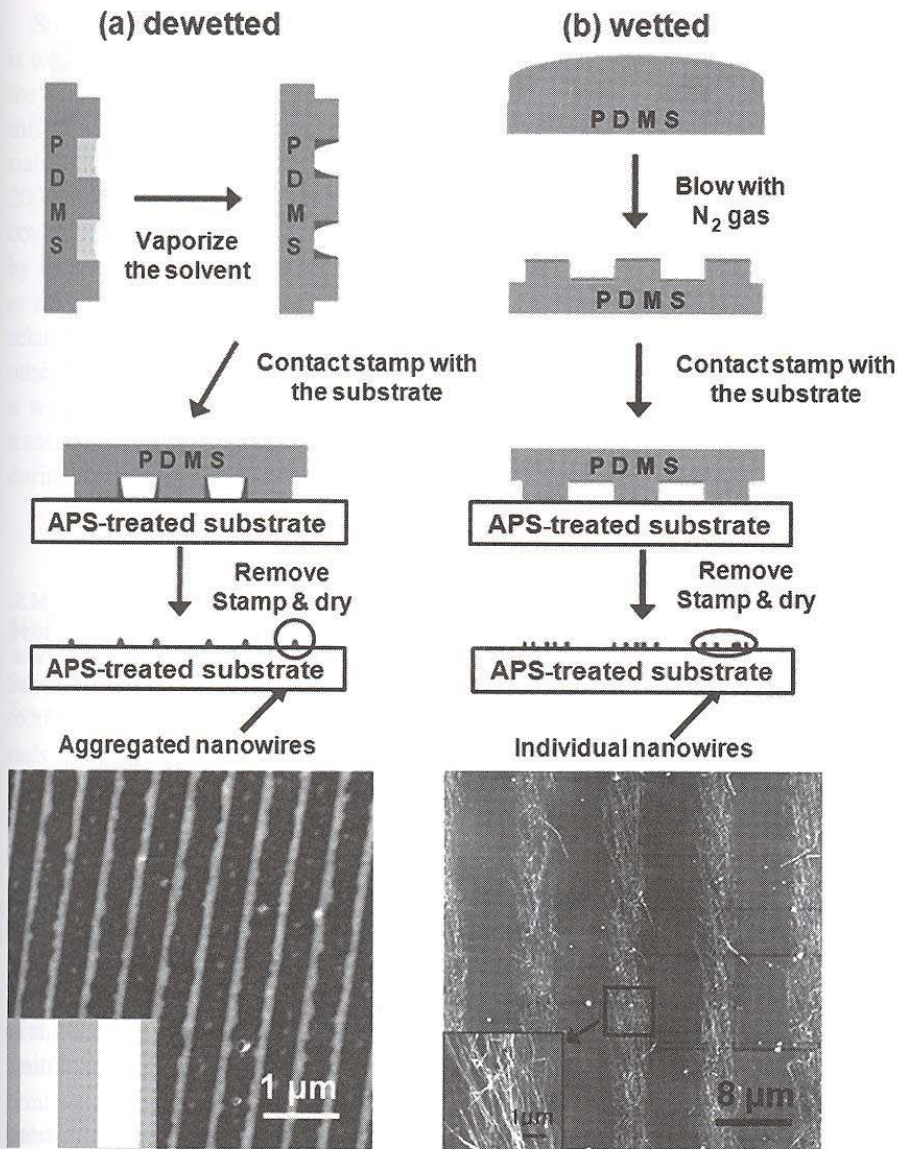
Fig. 10.7 MCP using a V_2O_5 nanowire ink with (a) hydrophobic and (b) hydrophilic PDMS stamp (from Kim, Y.-K., Park, S.J., Koo, J.P., Oh, D.J., Kim, G.T., Hong, S. and Ha, J.S. (2006) *Nanotechnology* **17**, 1375 ©2006 Institute of Physics and IOP Publishing Limited, reprinted with permission).

transparency and a conductivity comparable to an ITO electrode (Fig. 10.8(b)) (Zhou *et al.* 2006; Hu *et al.* 2007). The Langmuir–Blodgett (LB) technique is very useful in the transfer of uniform molecular films formed via floating of amphiphilic molecules onto a water surface and controlling the surface area. Nanomatrial patterns can be also transferred via the LB technique. As shown in a Fig. 10.8(c), inking of patterned PDMS stamp with nanomaterial films on a water surface and subsequent direct printing onto the substrate could transfer the pattern (Santhanam *et al.* 2004; Park *et al.* 2007).

In the case of nanomaterials, which would not spontaneously float on a water surface to form a LB film, surface modification by surfactant (Kim *et al.* 2001; Tao *et al.* 2003; Whang *et al.* 2003) or formation of surfactant film to aggregate the nanomaterials (Yamaki *et al.* 2001; Park *et al.* 2007) could be done. Monolayer LB films of hexagonally ordered alkanethiol coated Au
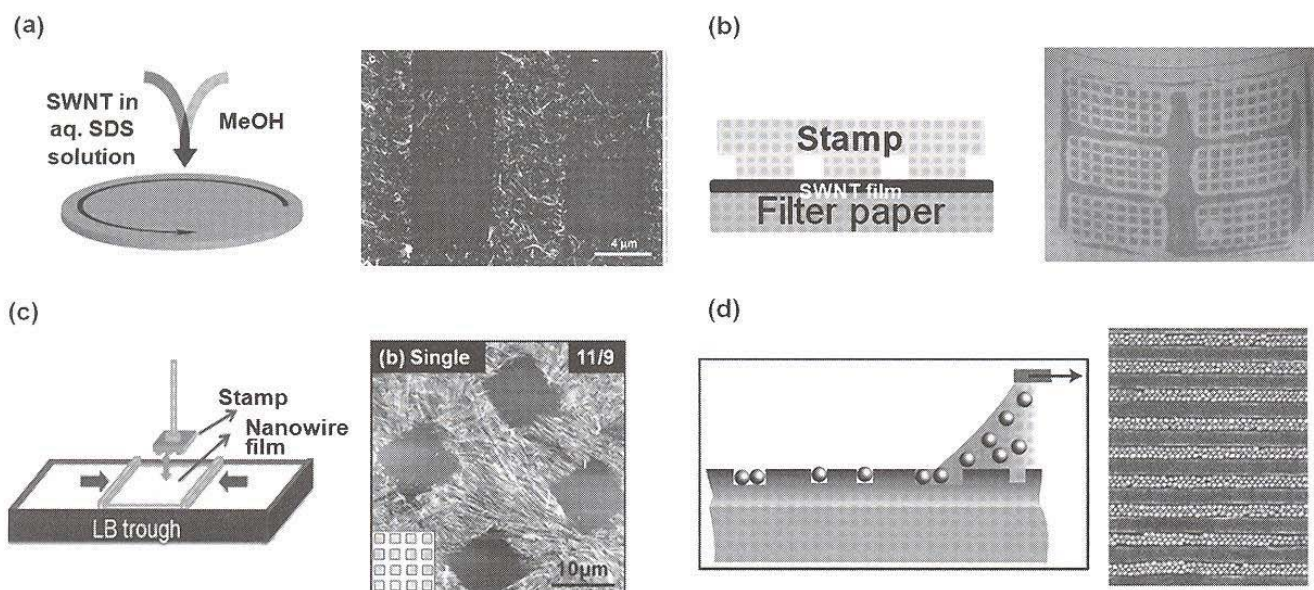
Fig. 10.8 Inking methods and the transferred patterns. (a) Spin coating (from Meitel, M.A., Zhou, Y., Gaur, A., Jeon, S., Usrey, M.L., Strano, M.S. and Rogers, J.A. (2004) *Nano Lett.* **4**, 1643 ©2004 American Chemical Society, reprinted in part with permission). (b) Direct transfer of filtered SWNT film (from Zhou, Y., Hu, L. and Grüner, G. (2006) *Appl. Phys. Lett.* **88**, 123109 ©2006 American Institute of Physics, reprinted in part with permission). (c) Langmuir–Schaefer technique (from Park, J., Shin, J. and Ha, J.S. (2007) *Nanotechnology* **18**, 405301 ©2007 Institute of Physics and IOP Publishing Limited, reprinted with permission). (d) Dewetting (from Kraus, T., Malaquin, L., Schumid, H., Riess, W., Spencer, N.D. and Wolf, H. (2007) *Nature Nanotech.* **2**, 570 ©2007 Nature Publishing Group, reprinted in part with permission).

nanoparticles were also transferred (Park *et al.* 2007). Transfer of the one-dimensionally aligned nanowire patterns without any deformation could be done in this way, too (Kim *et al.* 2001; Tao *et al.* 2003; Whang *et al.* 2003). Figure 10.8(d) shows the selective inking of Au nanoparticles onto the groove area of the stamp by hydrodynamic and surface forces (Kraus *et al.* 2007). Moving the meniscus of a colloidal Au suspension over the patterned PDMS stamp made the arrangement of dispersed Au particles inside the grooves. It is attributed to the dewetting properties of the stamp. Single-particle resolution was obtained by controlling the pattern size of the stamp.

In MCP using a patterned stamp, transfer of the nanomaterials onto substrate as well as the inking of nanomaterials onto the stamp is very important. Attractive interaction between the ink materials and the stamp is very helpful in the inking process, but may be disadvantageous in the transfer of ink onto substrates. Except for the cases of chemical bonding and the transfer of charged materials, the transfer of the nanomaterials onto the substrates can be explained in terms of the work of adhesion calculated from the surface energy between stamp, nanomaterials, and the substrate (Adamson *et al.* 1997; Wang *et al.* 2003). When the force of adhesion between the nanomaterials and the substrate is stronger than that between the stamp and nanomaterials, nanomaterials can be spontaneously transferred onto the substrate. Individual surface energy can be easily calculated from the Young's equation and Wendt equation by measuring the contact angles (Adamson *et al.* 1997; Wang *et al.* 2003). This mechanism of pattern transfer could be applied to the selective removal of thin films by a stamp on top of the film as well as to the transfer printing of organic materials such as pentacene (Wang *et al.* 2003; Choi *et al.* 2005).

Surface modification by oxidation or coating of self-assembled monolayers is usually used to enhance the transfer rate by improving the adhesion between the nanomaterials and substrate, to enhance the resolution by hindering the diffusion of inks on the substrate, and to prohibit the aggregation of nanomaterials due to repulsive interaction between the substrate and the ink (Meitl *et al.* 2004; Hu *et al.* 2007; Kim *et al.* 2007). Amine-termination of SiO_2 surface could help the complete transfer of V_2O_5 nanowires and enhance the resolution by increasing the interaction between V_2O_5 nanowires and the substrate (Kim *et al.* 2007). However, pattern transfer is not simply explained just by the relative interaction between the stamp, nanomaterials, and the substrate. So, other factors such as viscosity and gravity should be considered. Recently, it was reported that ink materials could be either picked up by the stamp or transferred onto the substrate by change of the speed of peeling off the stamp during the printing process (Meitl *et al.* 2006; Feng *et al.* 2007).

10.2.3 Other printing methods of nanostructures

Semiconducting one-dimensional (1D) materials such as SWNT, Si, and metal-oxide nanowires have been extensively studied as promising component materials of future nanoelectronic devices (Li *et al.* 2006; Wang *et al.* 2007). 1D nanomaterials are expected to be applied to the future flexible devices due to their flexibility as well as their high electrical mobility (Hong *et al.* 2007; Ju *et al.* 2007). For the fabrication of actual devices, a patterning process of nanowires as well as the synthesis of high-quality nanowires should be established. Control of the position and alignment can enhance the device performance and the uniformity as well as the stability of the devices (Pimparkar *et al.* 2007). In this section, we will focus on the transfer-printing methods extended from the traditional MCP, where the materials printed from the stamp actually function in organic optoelectronics or other applications. Transfer-printing methods are simple, economical, processed under the mild conditions to be applied to the flexible substrates (Hong *et al.* 2007), and the resolution would exceed that of traditional MCP.

Via a transfer-printing method, nanowires and nanotubes grown or aligned on the mother substrates could be selectively transferred onto the substrate without change of properties and the alignment. Figure 10.9(a) shows the patterning process of microstructured single-crystalline Si ribbon, fabricated on the mother-substrate via a top-down method, onto the flexible PET substrate via a transfer-printing technique (Lee *et al.* 2005). Inking on the relief area of the stamp was performed by contacting the microstructures with a patterned PDMS stamp, and the transfer of the microstructured Si to PET was done by contacting the inked stamp on the PET substrate coated with UV-curable polyurethane (PU) and exposure to UV. This technique enabled the fabrication of high-performance devices based on high-quality microstructures from single-crystalline Si wafers (Menard *et al.* 2004; Lee *et al.* 2005; Sun *et al.* 2005; Baca *et al.* 2007), GaAs (Sun *et al.* 2004), and GaN (Lee *et al.* 2006a) and the SIO substrate via combination of top-down and bottom-up processes.
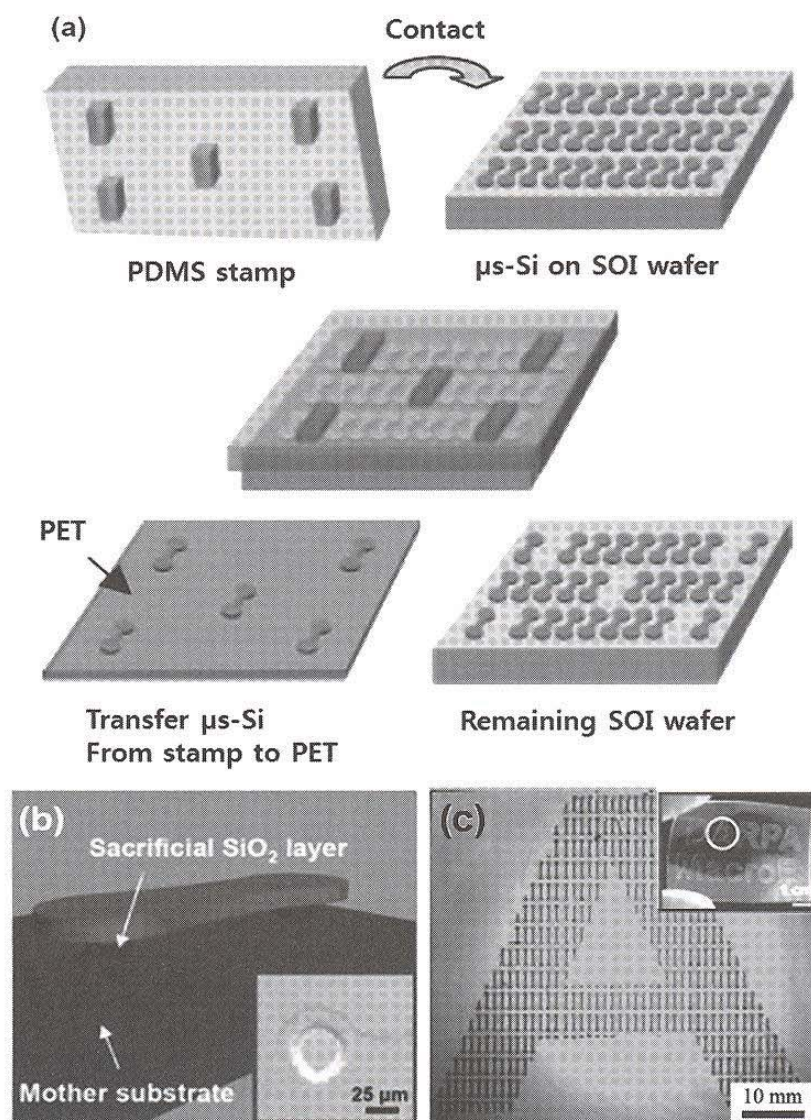
Fig. 10.9 (a) Schematics of selective transfer of microstructured Si onto PET by using PDMS stamp. (b) Sacrificial SiO$_2$ layer for pattern transfer. (c) Letter "A" composed of microstructured Si (from Lee, K.J., Motala, M.J., Meitl, M.A., Childs, W.R., Menard, E., Shim, A.K., Rogers, J.A. and Nuzzo, R.G. (2005) *Adv. Mater.* **17**, 2332 ©2005 Copyright Wiley-VCH Verlag GmbH & Co. KGaA., reproduced with permission).

Aligned nanowire films can be also obtained via printing of the inked stamp after transfer of the nanowires, grown on the mother substrate with an alignment, onto the stamp. That is a transfer technique of nanowires grown aligned on the mother substrate to the substrate for the nanodevice fabrication. Figure 10.10(a) shows transfer printing of CVD-grown perfectly aligned SWNTs onto the substrate (Kang *et al.* 2007a). Deposition of 100-nm thickness gold and coating of polyimide onto CVD-grown SWNTs was done. Au layers worked as an encapsulation of SWNTs for their successful transfer from the quartz substrate onto the stamp and the polyimide enhanced the transfer of SWNTs by improving the contact with PDMS. Printing of an inked stamp onto the substrate and sequential removal of polyimide and Au resulted in the aligned SWNT films without any deterioration form the mother substrate.

Various SWNT structures of cross and triangular junction could be obtained by repetition of the printing process on the same substrate and the fabrication of SWNT patterns in the desired position could also be done by additional
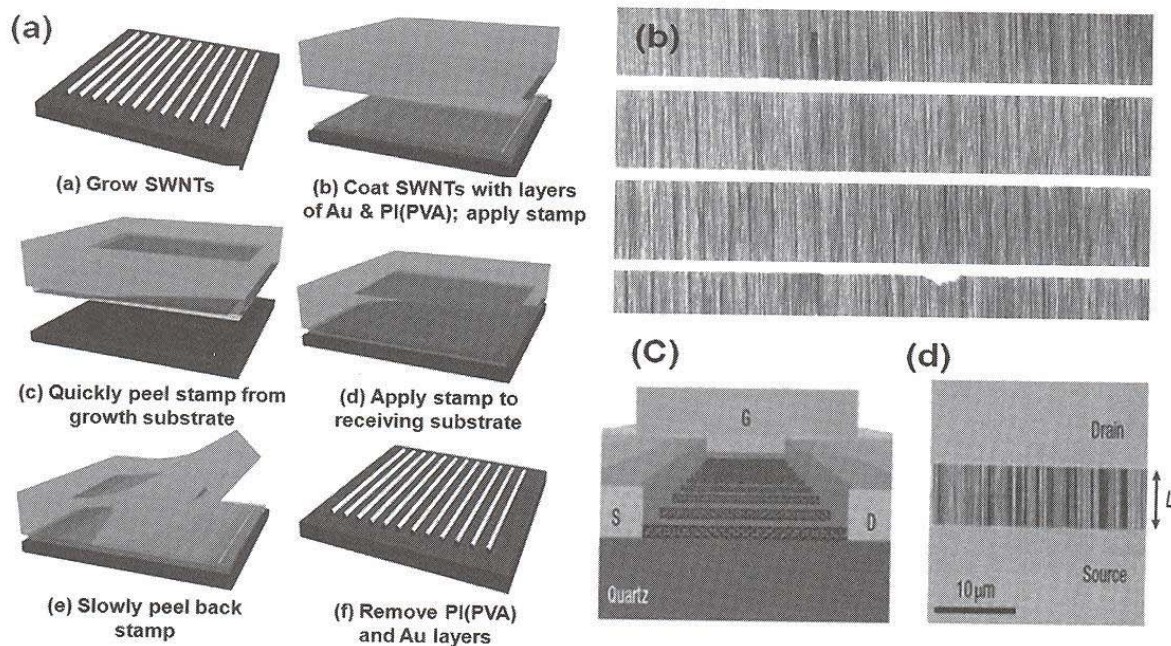
Fig. 10.10 (a) Schematics of the transfer of grown SWNTs (from Kang, S.J., Kocabas, C., Kim, H.-S., Cao, Q., Meitl, M.A., Kang, D.-Y. and Rogers, J.A. (2007a) *Nano Lett.* **7**, 3343 ©2007 American Chemical Society, reprinted in part with permission). (b) SEM image of transferred SWNTs (c) Schematic of SWNT FET (d) SEM image of aligned SWNT channel region (from Kang, S.J., Kocabas, C., Ozel, T., Shim, M., Pimparkar, N., Alam, M.A., Rotkin, S.V. and Rogers, J.A. (2007b) *Nature Nanotech.* **2**, 230 ©2007 Nature Publishing Group, reprinted in part with permission).

photolithography and reactive ion etching processes. FET devices of aligned SWNTs showed a mobility of ~1000 cm^2 V^{-1} s^{-1}. Such a transfer-printing technique is expected to be applied to the transfer of other materials onto the device substrates, regardless of their alignment.

Besides the fabrication of aligned nanowire patterns by using the originally aligned nanowires, unidirectional alignment of the nanowires from the randomly grown nanowires could be induced by intentional force during the contact-printing process. It is attributed to the anisotropic 1D structure of nanowires. As mentioned earlier, nanowires can be aligned perpendicular to the compression direction of the barrier in the LB trough (Kim *et al.* 2001; Tao *et al.* 2003; Whang *et al.* 2003) and they can be aligned along the flow of the carrier solvent inside the microfluidic channel (Messer *et al.* 2000; Huang *et al.* 2001; Park *et al.* 2006a). Figure 10.11(a) shows the patterning of nanowires via contact printing of the nanowire grown substrate onto the substrate (Javey *et al.* 2007; Fan *et al.* 2008).

The donor substrate was contacted with the patterned substrate after the growth of the Ge/Si core/shell nanowires by CVD, and then it was pushed along the direction of the desired alignment of nanowires. During this process, nanowires are transferred onto the substrate and they are aligned by the sheer stress. Here, the cutting of nanowires due to the friction between two substrates could be prohibited by addition of a lubricant, a mixture of octane and mineral oil (Fan *et al.* 2008).
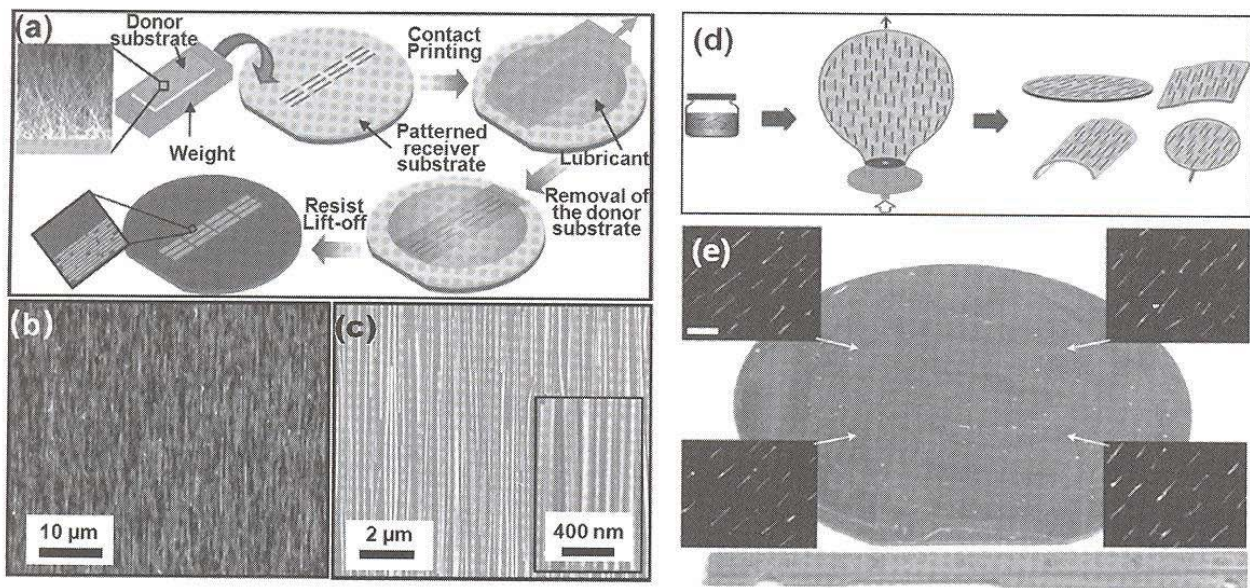
Fig. 10.11 (a) Contact printing of nanowire arrays, (b) Optical image and (c) SEM image of Ge nanowires (from Fan, Z., Ho, J.C., Jacobson, Z.A., Yerushalmi, R., Alley, R.L., Razavi, H. and Javey, A. (2008) *Nano Lett.* **8**, 20 ©2008 Institute of Physics and IOP Publishing Limited, reprinted with permission). (d) Blowing-bubble process of SWNT alignment (e) Transferred aligned SWNTs on Si wafer (from Yu, G., Cao, A. and Lieber, C.M. (2007) *Nature Nanotech.* **2**, 372 ©2007 Nature Publishing Group, reprinted in part with permission).

Figure 10.11(b) shows the transfer of well-aligned Si nanowires onto 6″ wafer substrate (Yu *et al.* 2007); alignment of the randomly dispersed emersion of Si nanowires could be done by extension stress during the blowing-bubble process and then the aligned Si nanowire patterns could be transferred by contact of the substrate onto the bubble. Such an alignment of randomly dispersed nanowires would be very useful in mass production.

Recently, three-dimensional multilayer stacks of nanowire arrays were fabricated (Ahn *et al.* 2006; Javey *et al.* 2007). Figure 10.12(a) shows the schematics of the fabrication of multistack structured devices. A maximum 9-layered device on the flexible substrate was fabricated via patterning of nanowires by transfer printing and repeated deposition of gate dielectric materials, insulating layers, or metal electrodes. The device performance on each level was uniform (Javey *et al.* 2007) and it was not deteriorated after repetition of bending. Heterogeneous three-level devices of SWNT, GaN, and Si nanoribbons were also fabricated (Ahn *et al.* 2006), where the interlayer alignment by $\sim$2 μm was controlled by using the transfer-printing apparatus as shown in Fig. 10.12(e). Inverters by connecting the interlayer devices as well as the MOSFETs in a unilevel structure were fabricated in this way and showed a stable performance on bending. These printing-based patterning techniques can produce a wide range of multilayer and multifunctional 3D electronics in the future. Micro-contact printing, expected to replace the photolithography, is behind the other lithography techniques in the competition of minimum feature sizes, due to unexpected disadvantages. However, it will continue to play an important role in the fabrication of future electronic devices based on nanomaterials, owing to its simplicity, low cost, mild processing condition and wide applications to various nanomaterials.
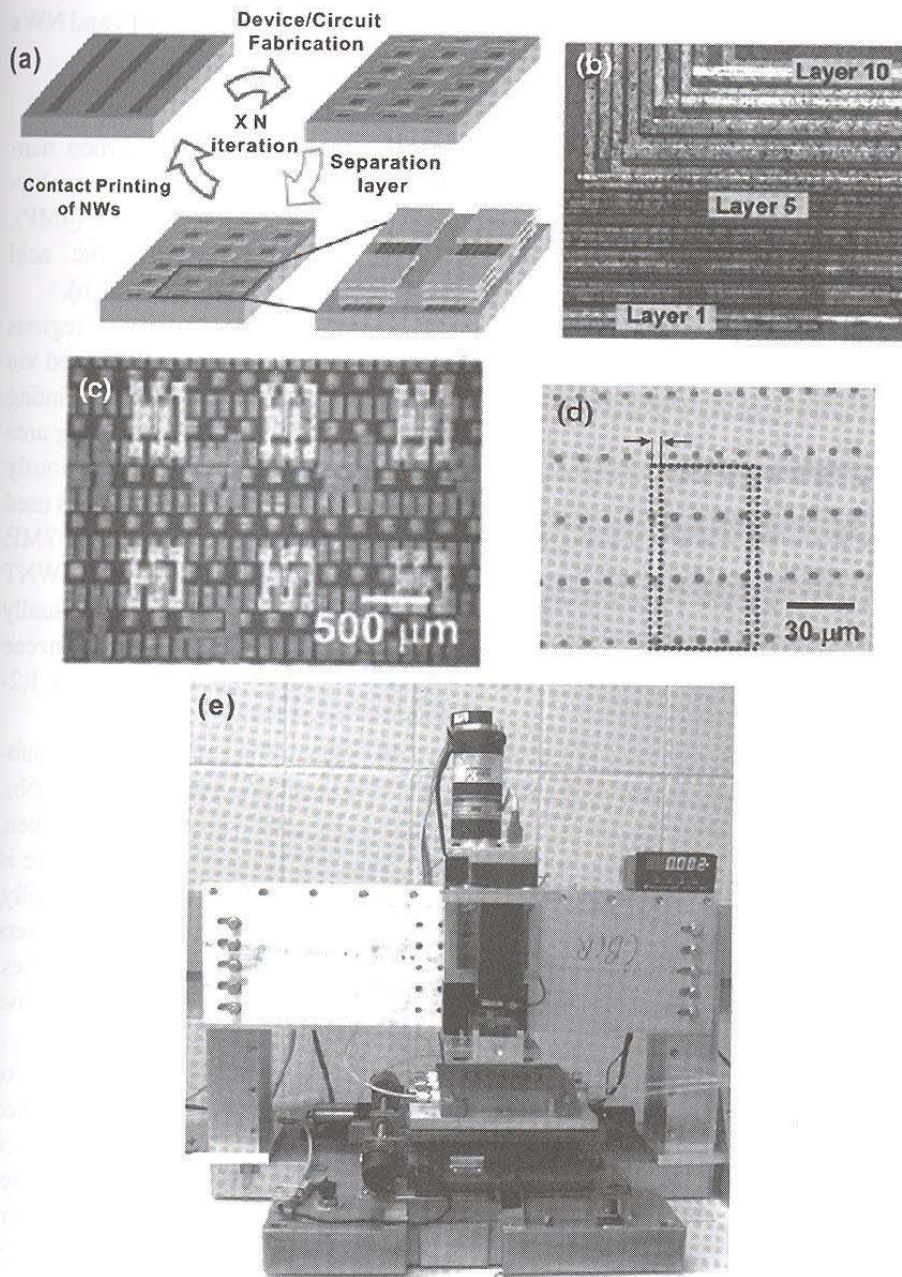
Fig. 10.12 (a) Schematic of 3D nanowire circuit fabrication, (b) 10 layers of Ge/Si nanowire FETs (from Javey, A., Nam, S.W., Friedman, R.S., Yan, H. and Lieber, C.M. (2007) *Nano Lett.* **7**, 773 ©2007 American Chemical Society, reprinted in part with permission). (c) 3D heterogeneously integrated electronic device, (d) Aligned 2-layer printed structure, (e) Automated stage for transfer printing (from Ahn, J.H., Kim, H.-S., Lee, K.J., Jeon, S., Kang, S.J., Sun, Y., Nuzzo, R.G. and Rogers, J.A. (2006) *Science* **314**, 1754 ©2006 American Association for the Advancement of Science, reprinted with permission).

10.3 Directed assembly of nanostructures

10.3.1 Directed assembly procedure

In this section, we describe a large-scale directed self-assembly process of nanostructures (Rao *et al.* 2003) without use of any external forces. Here, the substrate potential can be used to only further enhance the nanotubes (NTs) and nanowires (NWs) adsorption. This new assembly strategy is often called the "surface programmed assembly (SPA)" process (Hong *et al.* 2008). It is comprised of two simple steps: surface molecular patterning and

surface-directed assembly of nanostructures. Using this method, NTs and NWs can be assembled onto specific locations of solid substrates.

10.3.1.1   *Carbon nanotubes*

Im *et al.* performed a SPA process to assemble single-walled carbon nanotubes (SWNTs) on various polar and non-polar self-assembled monolayers (SAMs) such as 2-mercaptopyridine (2MP), 4-mercaptopyridine (4MP), 2-mercpatoimidazole (2MI), cysteamine, 16-mercaptohexadecanoic acid (MHA) and 1-octadecanethiol (ODT) (Fig. 10.13(a)) (Im *et al.* 2006a,b).

The SAM was patterned onto the Au substrate to create surface regions with different polarities. At first, the first molecular species are patterned via DPN (Hong *et al.* 2000; Ivanisevic *et al.* 2001) or the microcontact printing (MCP) method (Kumar *et al.* 1993; Xia *et al.* 1998), and the remaining area is backfilled with the second molecular species by dipping the previously patterned substrate in the solution of the second molecules. Here, MHA is used for negatively charged areas and ODT for neutral regions. Cysteamine, 2MP, 4MP and 2MI are utilized to create positively charged surfaces. For SWNT assembly, the patterned substrate is placed in the SWNT suspension, usually for 10 s. Then, the substrate is rinsed thoroughly with 1,2-dichlorobenzene to remove extra SWNTs since the solution of SWNTs is dispersed in 1,2-dichlorobenzene.

Lee *et al.* also reported the assembly of SWNTs onto various pristine substrates without any linker molecules using a similar method (Lee *et al.* 2006b). In this process, photoresist is first patterned onto solid substrates. And then, the substrate is rinsed with anhydrous hexane. After rinsing, the substrate is immediately dipped into the OTS solution for selective passivation. Finally, the photoresist is removed with acetone. Such a patterning of OTS layers results in some neutral regions and other bare surface regions on the substrates. The patterned substrate is then placed in a solution of SWNTs for selective assembly (Fig. 10.13(b)).

Furthermore, electric potential can be used to increase the adsorption of SWNTs (Fig. 10.14). However, the final assembled structures of adsorbed SWNTs are still completely determined by surface molecular patterns. Since electric potential is used only to control the amount of adsorbed SWNTs, precise alignment of SWNTs even with applied bias voltage can be possible. This SPA process can also be utilized to assemble double-walled carbon nanotubes (DWCNT) and multiwalled carbon nanotubes (MWCNT).

10.3.1.2 V_2O_5 *nanowire*

Myung *et al.* demonstrated precise assembly and alignment of V_2O_5 nanowire arrays and nanowire-based devices over a large surface area ($\sim 1\,cm \times 1\,cm$) (Myung *et al.* 2005). Specifically, positively charged surface molecular patterns are utilized to assemble and align V_2O_5 NWs over a large area. The neutral molecular patterns are utilized to avoid the adsorption of nanowires (Figs. 10.15(a)–(d)).

A molecular patterning process is performed similarly by patterning the first molecular species via DPN, MCP or photolithography (Jaeger 2002; Busnaina 2007) as discussed before, and then the remaining area is backfilled with the second molecular species by a dipping process. The photolithography
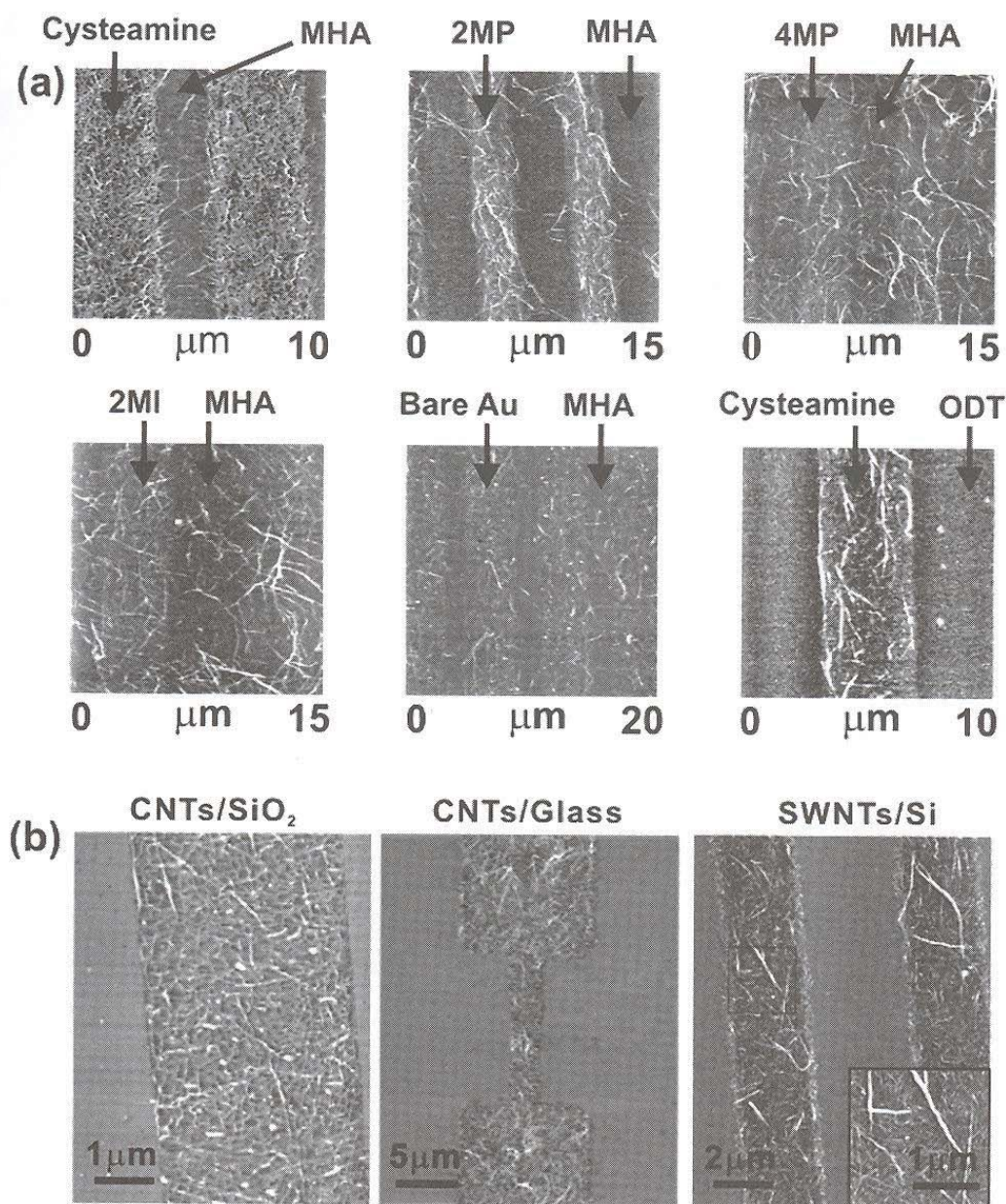
Fig. 10.13 (a) AFM topography images of SWNT patterns adsorbed onto SAM patterns comprised of: cysteamine and MHA, 2MP and MHA, 4MP and MHA, 2MI and MHA, 4MP and 2MI, 2MI and ODT. These patterns cover large surface area (∼1 cm × 1 cm) of the samples (from Im, J., Lee, M., Myung, S., Huang, L., Rao, S.G., Lee, D.G., Koh, J. and Hong, S. (2006) *Nanotechnology*, **17**, 3569, ©2006 Institute of Physics and IOP Publishing Limited, reproduced with permission). (b) SWNT networks formed directly on bare SiO₂ (left), glass (middle) and Si (right). OTS was used as the non-polar layer (from Lee, M., Im, J., Lee, B.Y., Myung, S., Kang, J., Huang, L., Kwon, Y.-K. and Hong, S. (2006) *Nature Nanotech.* **1**, 66 ©2006 Nature Publishing Group, reproduced in part with permission).

method is utilized to create large-scale molecular patterns comprised of 1-octadecyltrichlorosilane (OTS) for the neutral region and aminopropylethoxysilane (APTES) for positively charged patterns on SiO₂. In this case, photoresist is first patterned on SiO₂, and the substrate is placed in the OTS solution (1:500 v/v in anhydrous hexane) for coating the bare SiO₂ regions.
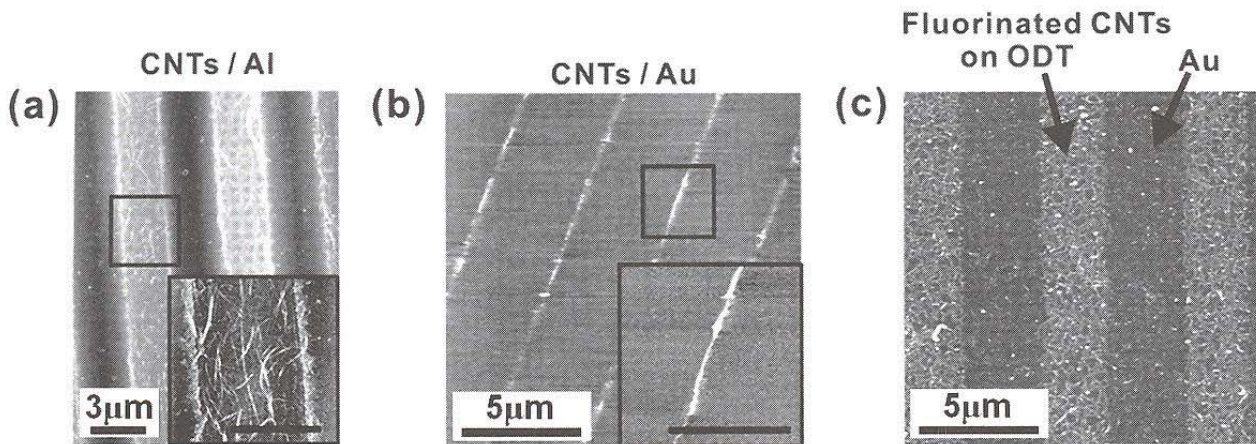
Fig. 10.14 (a) SWNTs selectively adsorbed onto bare Al surfaces with a substrate bias of -1.5 V. OTS was used for passivation. (b) High-precision alignment of SWNTs onto Au surfaces with -1 V substrate bias. ODT was used as the non-polar layer. (c) Fluorinated SWNTs adsorbed onto ODT regions with -3 V substrate bias (from Lee, M., Im, J., Lee, B.Y., Myung, S., Kang, J., Huang, L., Kwon, Y.-K. and Hong, S. (2006) *Nature Nanotech.* **1**, 66 ©2006 Nature Publishing Group, reproduced in part with permission).

After the photoresist is removed with acetone, the substrate is dipped into APTES solution (1:500 v/v in ethanol) to backfill the remaining SiO_2 area.

When the patterned substrates are placed in an aqueous solution of V_2O_5 NWs for ~ 30 s, NWs are attracted toward the positively charged molecular regions, and aligned along the molecular patterns due to the negatively charged property of V_2O_5 NWs (Fig. 10.15(c)). The substrate is then rinsed with thoroughly deionized water to remove any extra NWs. For Au substrate, SAM patterns are prepared using cysteamine as positively charged patterns and ODT for neutral regions, and successfully assembled a large number of pristine NWs over a 1 cm $\times$ 1 cm area (Figs. 10.15(a), (b), (d)). Since V_2O_5 NWs do not adhere to bare Si or SiO_2 surfaces without a bias voltage, electric potential can also be utilized to enhance the adsorption of NWs. As V_2O_5 NWs are charged negatively in aqueous solution, we could assemble them by applying positive substrate bias voltage. Furthermore, even individual V_2O_5 NWs can be assembled in small patterns on the substrates with the help of electric potential (Fig. 10.15(e)).

10.3.1.3   *ZnO nanowires*

Kang *et al.* also reported ZnO NW adsorption and alignment using a similar method as described above (Kang *et al.* 2008). First, on the Au surfaces, MHA is used to create negatively charged molecular patterns, while ODT is used for neutral regions. On SiO_2 substrates, the bare SiO_2 surface is used as a negatively charged surface, while OTS or octadecyltrimethoxysilane (OTMS) are first patterned for neutral regions, while leaving some bare SiO_2 regions. When the patterned substrate is placed in the ZnO NW solution for ~ 10 min, pristine ZnO NWs are attracted to the negatively charged region, and then assembled and aligned directly onto MHA region or the SiO_2 surface (Fig. 10.16). The substrate is then rinsed with deionized water to remove any extra NWs. Moreover, the amount of adsorbed ZnO NWs could also be enhanced by applying a negative bias voltage to the substrates as in the previous NTs and NWs assembly.
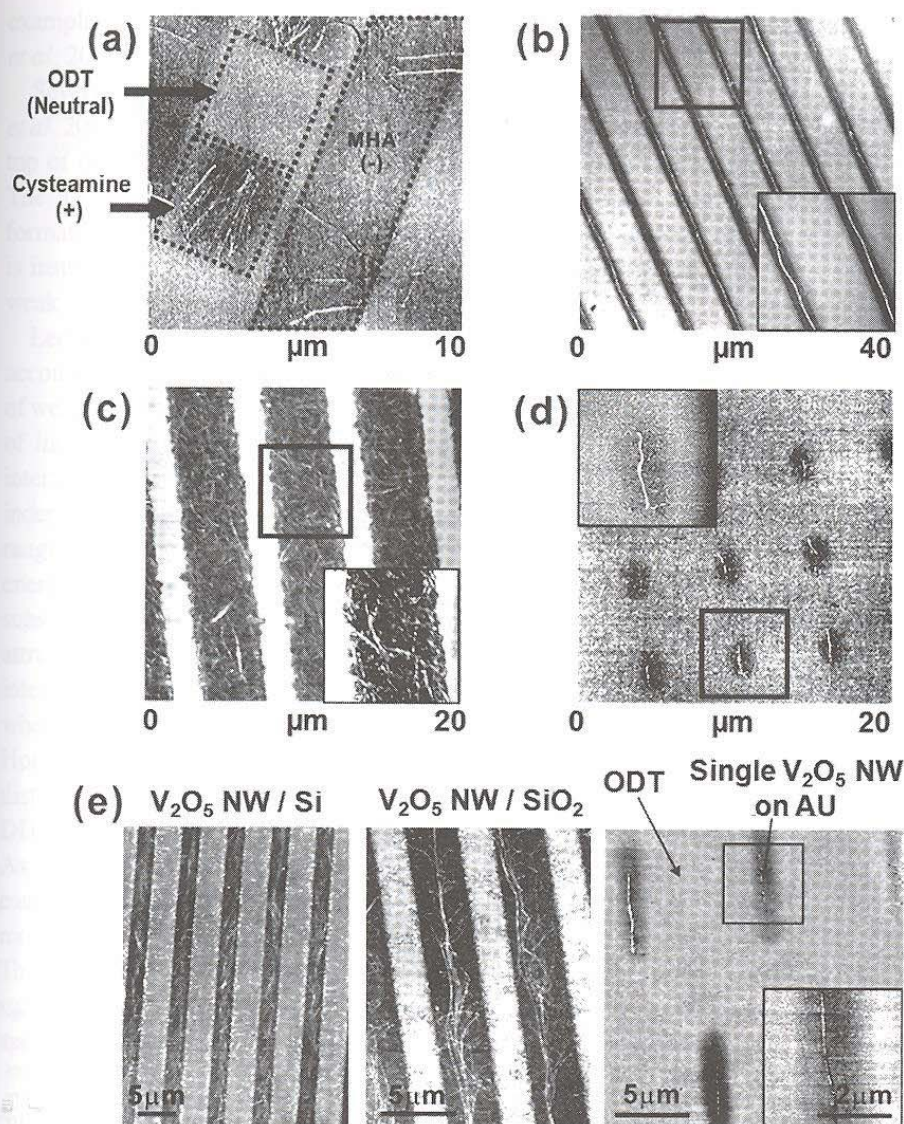
Fig. 10.15 (a) Atomic force microscopy (AFM) topography image of V_2O_5 nanowires assembled onto SAM patterns comprised of ODT (neutral), MHA (negatively charged), and cysteamine (positively charged). (b) AFM topography image of V_2O_5 nanowires (white lines) assembled on cysteamine patterns (dare areas) on Au. The remaining area was passivated with ODT (bright areas). (c) AFM topography image of V_2O_5 nanowires assembled on APTES patterns on SiO_2. OTS was utilized for passivation. Insets show high-resolution AFM images of OTS (left) and APTES regions (right), respectively. (d) AFM topography image of individual V_2O_5 nanowires (white lines) assembled on cysteamine patterns (dark areas) on Au. ODT (bright areas) was utilized for passivation (from Myung, S., Lee, M., Kim, G.T., Ha, J.S. and Hong, S. (2005) *Adv. Mater.* **17**, 2361 ©2005 John Wiley & Sons Limited, reproduced with permission). (e) V_2O_5 NWs selectively adsorbed onto bare Si (left) and SiO_2 (middle) surfaces using a substrate bias 3 V and 6 V, respectively. Individual V_2O_5 NWs directly adsorbed onto bare Au surfaces using 3 V substrate bias using ODT as the non-polar layer (from Lee, M., Im, J., Lee, B.Y., Myung, S., Kang, J., Huang, L., Kwon, Y.-K. and Hong, S. (2006) *Nature Nanotech.* **1**, 66 ©2006 Nature Publishing Group, reproduced in part with permission).

10.3.2   Mechanism of various assembly processes of nanostructures

In this section, we discuss a theoretical model describing the collective behavior of molecules in direct deposition processes such as dip-pen nanolithography and other directed assembly procedures. Interplay between intermolecular interactions and substrate–molecule interactions may result in diverse shapes of molecular patterns. Computer simulations based on a simple model reveal circular and star-like patterns at low and intermediate densities of preferentially attractive surface sites, respectively. At a large density of such surface sites, the molecules form a two-dimensional invasion percolation cluster. We also discuss the self-assembly process of a long rod-like molecule on patterned substrate immersed in a two-dimensional sliding chamber.
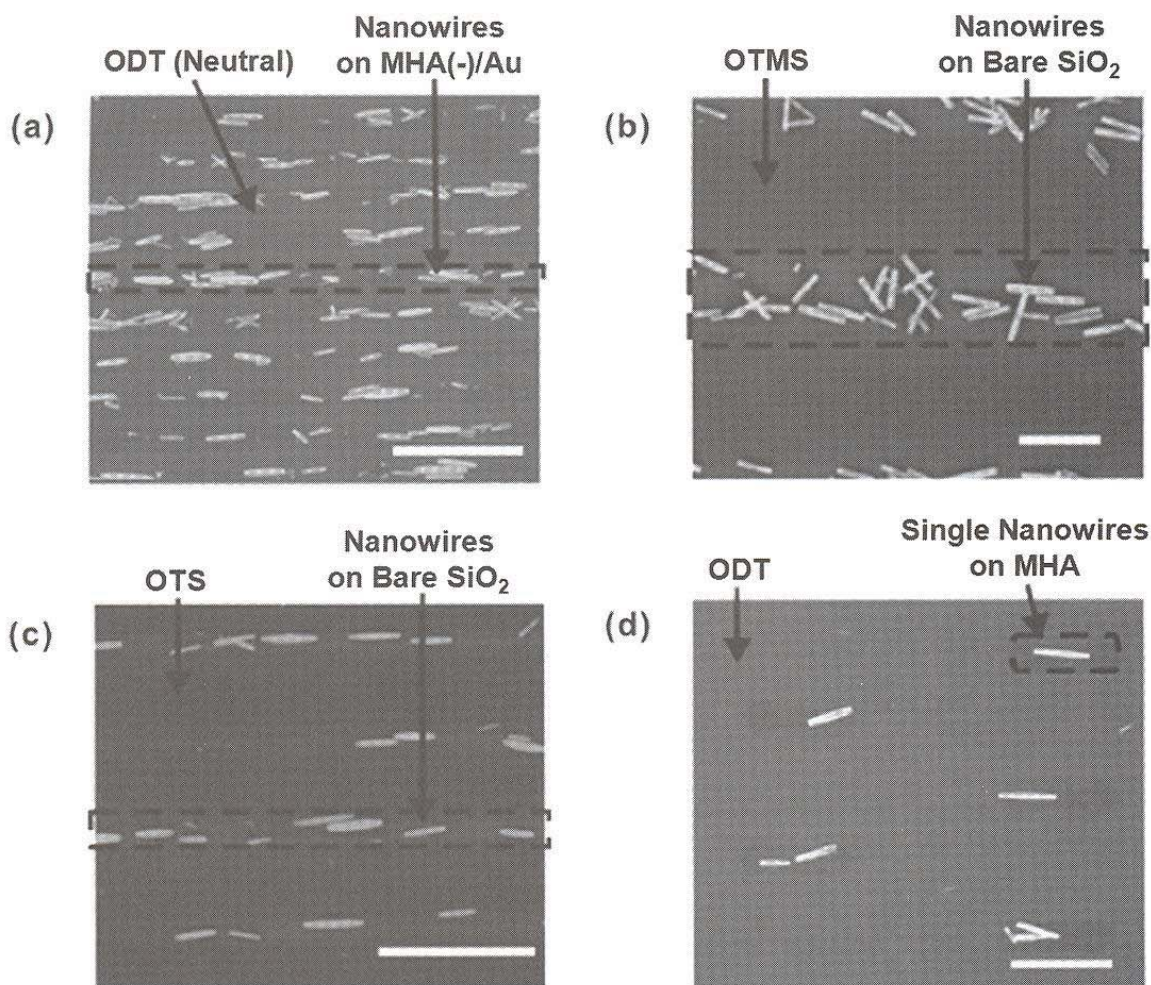
Fig. 10.16 Scanning electron microscopy (SEM) images and analysis results of ZnO NWs assembled on the various substrates via the solution-phase method. (a) ZnO NWs assembled on MHA line patterns on a Au substrate without a substrate bias voltage. The remaining area was passivated by ODT to prevent non-specific adsorption of ZnO NWs. The scale bar represents 20 μm. (b) ZnO NWs assembled directly onto bare SiO$_2$ surfaces without substrate bias voltage. OTMS SAM was utilized for passivation. The scale bar represents 5 μm. (c) ZnO NWs assembled directly onto bare SiO$_2$ surfaces without a substrate bias voltage. OTS SAM was utilized for passivation. The scale bar represents 20 μm. (d) Individual ZnO NWs assembled onto MHA patterns on Au without a substrate bias voltage. ODT was utilized for passivation. The scale bar represents 5 μm (from Kang, J., Myung, S., Kim, B., Oh, D., Kim, G.T. and Hong, S. (2008) *Nanotechnology* **19**, 095303 ©2008 Institute of Physics and IOP Publishing Limited, reprinted with permission).

10.3.2.1   *Modelling of collective behavior*

In a common DPN process, a molecule-coated AFM tip is held at a fixed position in contact with the substrate so that molecules flow onto the substrate to form various-size "dot" patterns. Various direct deposition experiments show that if deposited molecules strongly bind to the substrates, the pattern always grows in a circular shape (Piner *et al.* 1999; Hong *et al.* 2000; Rozhok *et al.* 2003; Ginger *et al.* 2004; Peterson *et al.* 2004). Examples include alkanethiol molecules on gold. On the other hand, when the binding to the substrates is relatively weak compared to the attractive molecule–molecule interactions, non-circular patterns are often observed. Most representative patterns are fractal-like patterns with the fractal dimension of ~1.51 when 1-dodecylamine (DDA) molecules are deposited onto mica (Manandhar *et al.* 2003). Other

examples include proteins and conducting polymers (Wilson *et al.* 2001; Lim *et al.* 2002).

Several theoretical models (Jang *et al.* 2001; Sheehan *et al.* 2002; Weeks *et al.* 2002) describe the motion of deposited molecules as Fickian diffusion on top of other molecular layers until they covalently anchor to bare substrates. The application of this model seems to be limited to the circular pattern formation of strong surface-binding molecules. Obviously, the diffusion model is insufficient to explain non-circular pattern formation, which is common in weak surface-binding cases.

Lee and Hong (2006) proposed a theoretical model that successfully accounts for diverse shapes of molecular patterns in dip-pen nanolithography of weak-binding molecules. In this model, the focus has been placed on the role of intermolecular interactions and inherent non-uniform substrate–molecule interactions. In contrast to previous models where deposited molecules diffuse independently, here the motion of molecules is identified as collective rear-rangements of a cluster whose periphery adapts its shape to form the minimum energy state for all. The deposited molecules bind weakly onto most of the substrate regions except for several impurity sites on substrates. Furthermore, attractive intermolecular interactions combine all molecules together. The interactions with strong binding sites result in non-trivial pattern formation when molecules aggregate via attractive intermolecular interactions. Lee and Hong have pointed out that for charged molecules such as DDA, randomly distributed surface charges on mica play roles as strong binding sites. For DDA, molecules are attracted to each other due to hydrophobic interactions. As the molecules are preferentially attracted to certain surface sites, the tension can be released by making a channel toward the strong binding sites where molecules can flow in. The frontier moves by invading local areas in bursts. The frontier will become circular again unless it encounters any other attractive surface sites. When the frontier encounters other attractive sites, a new branch appears on the top of the growing branch.

Computer simulations based on a simple model taking into account the above feature demonstrate various self-assembly patterns (Lee and Hong 2006). The molecules live on two-dimensional hexagonal lattices. Each lattice site can be denoted using the index (i, j). The growth starts from the center by occupying neighboring sites that provide the maximum energy gain. When there are multiple minimal energy sites, the closest to the center becomes occupied first. The Hamiltonian of a cluster with M deposited molecules is

$$\frac{H}{k_B T} = -\sum_{\{i,j\}}^{M} \varepsilon_p s_{i,j} (s_{i,j+1} + s_{i,j-1} + s_{i-1,j+1} + s_{i+1,j-1} + s_{i+1,j} + s_{i-1,j})$$

$$+ \sum_n V(|R_{i,j} - r_n|),$$

where ε_p is the energy gain by pairwise interactions between molecules, and it contributes to the total energy gain only when two molecules are next to each other. The s_{ij} is an Ising-type variable indicating the occupancy of the corresponding site. $V(r)$ is the potential energy of a molecule at distance r apart from the strong surface binding site. r_n and $R_{i,j}$ are the position of

Fig. 10.17 Schematic representations of a cluster growth on hexagonal lattices. A deposited molecule may occupy a new sites (o) by creating (a) 3 pairs, (b) 2 pairs, (c) 1 pair of intermolecular contacts and (d) by advancing toward a strong binding site (*).
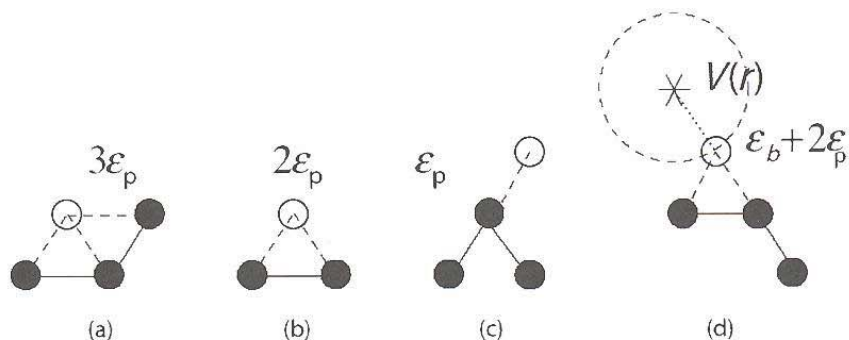
the nth strong-binding site and that of the molecule at the lattice site (i, j), respectively.

Figure 10.17 demonstrates the advance of the cluster frontiers. The energy gain by advancing from a concave boundary (Fig. 10.17(a)), a flat boundary (Fig. 10.17(b)), and a convex site (Fig. 10.17(c)) are $3\varepsilon_p$, $2\varepsilon_p$, and ε_p, respectively. Thus, the growing frontier has a tendency to fill the concave site first, leading to a circular-shape frontier. When a molecule is within the interaction range $r_b(\geqslant b)$ with a strong binding site, the energy gain by growing into the direction of the strong-binding site is $\varepsilon_b + n\,\varepsilon_p$ where n is the number of intermolecular interaction pairs by making a bridge (Fig. 10.17(d)). Here, $\varepsilon_b = \delta V$ indicates the potential-energy gain at the periphery of the interaction range. If the substrate–molecule interaction wins over the line tension of the cluster boundary ($\varepsilon_b > \varepsilon_p$), the molecules can advance in the direction of the strong-binding site rather than filling an available concave site. The major parameters controlling the shape of the cluster growth are: (a) the number density of strong-binding sites and (b) the strength and range of the substrate–molecule and intermolecular interactions.

This simple but efficient framework can be applied for various DPN patterning experiments simply by plugging in proper parameters. As an example, we consider DDA molecules on mica, which can be a representative case of weak surface-binding molecules. DDA molecules have hydrophobic backbones with amine ($-NH_2$) end-groups. When deposited on mica, they aggregate among themselves via hydrophobic interactions and are bound rather weakly to the surface sites. Randomly distributed surface charges on mica act as strong binding sites and attract positively charged DDA molecules. The hydrophobic interaction is ~1 kcal/mol per methylene group. Thus, $\varepsilon_p \approx 10$ kcal/mol for a DDA pair consisting of 12 methylene groups provided that molecules are well aligned. Since mica surfaces are normally covered by a thin water layer, the Bjerrum length $l_B \equiv e^2/k_B T \approx 7$ Å in water sets the interaction range where the electrostatic interactions are active. The diameter of a deposited DDA molecule sets the lattice constant of the hexagonal lattices to be $b = 3$ Å. Thus, the "bridging" interaction range r_b is $l_B = 2b$ on the lattices. Considering that the typical strength of the electrostatic interaction at an atomic distance is 40–50 kcal/mol, we estimate the interaction strength $\varepsilon_b = \delta V$ at a Bjerrum length away to be about $2\varepsilon_p$. The reported surface charge density -0.34 C/m^2 (Pashley 1981) of mica corresponds to the number density $\sigma_s = 0.13$ on this
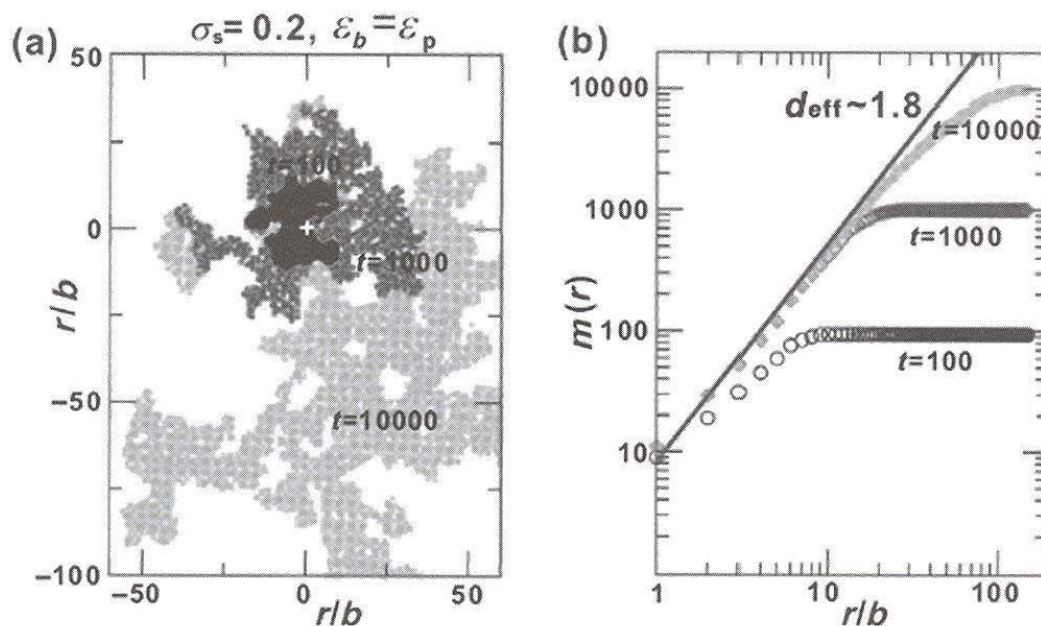
Fig. 10.18 (a) Cluster growth in invasion percolation regime. (b) The number of deposited molecules $m(r)$ inside of a circle of radius r.

hexagonal lattices ($b = 3$ Å). The simulation results using these parameters predict the growth of irregular-shape clusters similar to the reported DPN experiments using DDA molecules (Manandhar *et al.* 2003).

The parameters for simulations are extracted from various types of molecules. Figure 10.18 demonstrates cluster formation with $\sigma_s = 0.2$ and $\varepsilon_p = \varepsilon_b$. At this specific setup, the cluster growth resembles that of the *invasion percolation* process in fluid dynamics (Wilkinson *et al.* 1983). For instance, when water is injected slowly into a porous medium filled with oil, a water cluster grows with a fractal dimension of 1.82 (Furuberg *et al.* 1988). Here, the dynamics are determined by the capillary forces and the pore size. We measured the *effective* fractal dimension d_{eff} of each pattern by counting the number of molecules M at given $R \sim M^\nu$, $\nu = 1/d_{\text{eff}}$. Slopes in log–log plots depict the effective fractal dimension at given times. The measured fractal dimension of $\sim$1.8 for times $t \geqslant 10\,000$ is in agreement with the known fractal dimension of invasion percolation clusters. The growth direction is chosen by a few branches at the moment of a burst. The merging of these branches will destroy the hierarchy of fractal structures at later times. The invasion percolation cluster shape appears if the strong-binding site density is larger than a certain threshold σ_c so that the occupancy of a strong-binding site always guarantees filling neighboring binding sites before all concave sites around it.

The cluster shapes at various values of ε_p ε_b and σ_c are investigated. In the limit of strong intermolecule interaction ($\varepsilon_p \gg \varepsilon_b$), the molecules always aggregate into a trivial circular form. In the other limit ($\varepsilon_b \gg \varepsilon_p$), the cluster shape can be fractal-like patterns at lower density of strong-binding sites. Figure 10.18 demonstrates some representative cluster growth. For $\varepsilon_b \leqslant \varepsilon_p$ with small $\sigma_s = 0.13 < \sigma_c$, the overall shape is still circular (Fig. 10.19(a)). Molecules with strong intermolecular interactions fall into this category. At
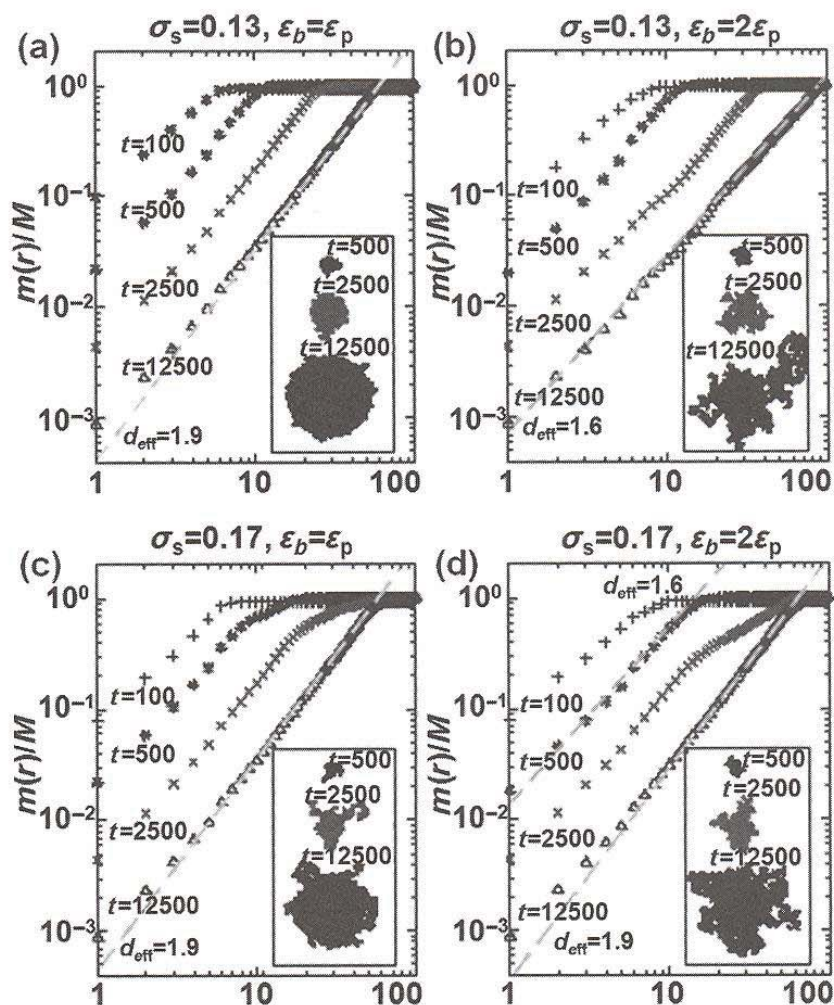
Fig. 10.19 Clusters (inserts) simulated with various surface charge densities, hydrophobic interactions, surface–molecule interactions. The cluster size $m(r)$ is the number of molecules with the range of r from the center. The slopes in the graph indicate the effective fractal dimension d_{eff}.

a larger substrate–molecule interaction $\varepsilon_b = 2\varepsilon_p$, we observe mixed patterns (Fig. 10.19(b)). At small times, branches and the central part are occupied with similar probabilities. At longer times, the outer branches continue developing but the central region no longer grows.

This is because, after the cluster size reaches a certain value, the lowest-energy sites are always found at the newly explored area. The measured fractal dimension is 1.6, which is similar to the reported value for DDA patterns on mica (Manandhar *et al.* 2003). It should be noted that the model parameters used in this simulation are extracted from the real interactions of DDA molecules.

For larger molecules (e.g. globular proteins), we can expect a different lattice constant. Consider molecules whose diameter is about 10% larger. Accordingly, the number density of strong-binding sites is scaled to $\sigma_s = 0.17$ (Figs. 10.19(c) and (d)). If $\varepsilon_b = \varepsilon_p$, the pattern shows the circular core and small branches. Boundary tension still suppresses the development of fractal-like structures. For $\varepsilon_b = 2\varepsilon_p$, branching is more favorable than occupying concave sites (Fig. 10.19(d)). These branches create new branches in a recursive way similar to the case $\sigma_s = 0.13$, $\varepsilon_b = 2\varepsilon_p$ (Fig. 10.19(b)), but they start
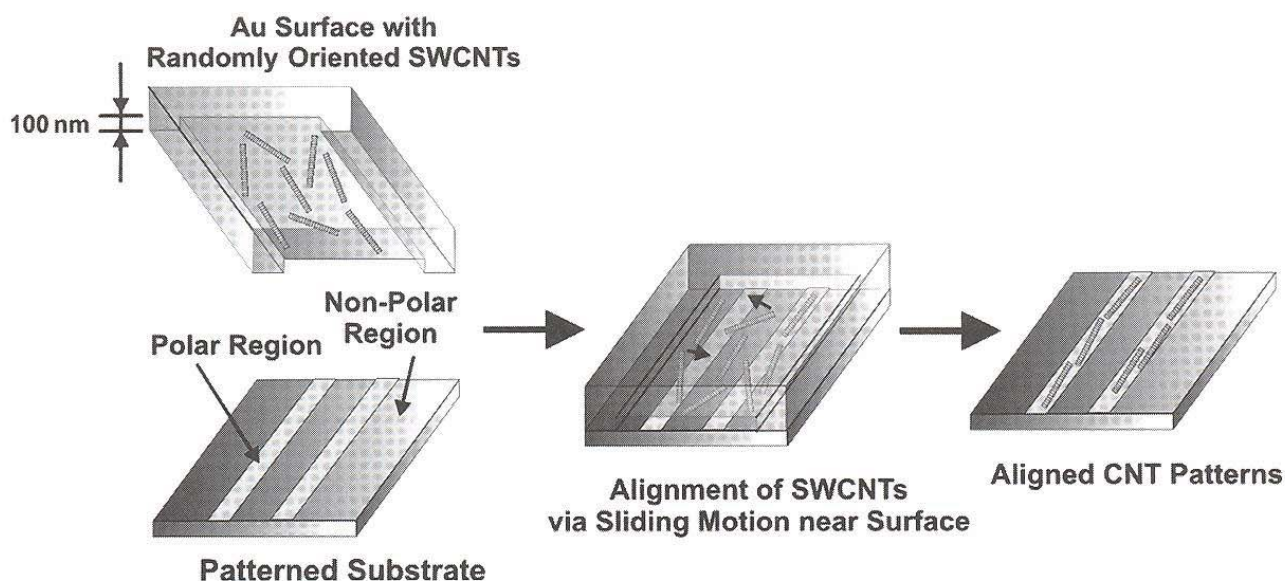
Fig. 10.20 Sliding reaction chamber experiment (from Im, J., Huang, L., Kang, J., Lee, M., Lee, D.J., Rao, S.G., Lee, N.-K. and Hong, S. (2006) *J. Chem. Phys.* **124**, 224707 ©2006 American Institute of Physics, reprinted in part with permission).

overlapping almost immediately. At earlier times ($t < 2500$), the growth can be anisotropic and shows the effective fractal dimension of ~ 1.6. It is not yet clear whether the cluster shape at this regime is fractal. At later times ($t > 2500$), the merged branches cover the substrates isotropically, resulting in the effective fractal dimension of ~ 2. A series of simulations on rectangular lattices reports similar behavior.

This model can also be generalized to strong surface-binding cases such as alkylthiolates on Au. In this case, all lattice sites are equally attractive to molecules. The simulation results show trivial circular patterns. One interesting situation is when strong-binding molecules can slide on the substrates due to the translation invariance. This effect can be taken into account by introducing a certain probability with which molecules can escape from the central aggregates. The escaped molecules may still diffuse on the substrate. The simulation results confirm a circular pattern with a blurred boundary, as observed in some DPN experiments (Sheehan *et al.* 2002).

10.3.2.2   *Self-assembly of long molecules*

We now discuss the adsorption of stiff rod-like molecules on patterned surfaces. Since long molecules have internal degrees of freedom that relax only at large timescales, the detailed description of kinetics is required to characterize the adsorption behaviors.

It is suggested that the selective adsorption of long polymer molecules can be used to create nanoscale devices. In particular, such molecules like CNT, DNA are extremely useful from the technological point of view. Various adsorption experiments of long molecules on a patterned surface have been carried out. In order to direct CNT or NWs, electric fields or external liquid flow have been utilized (Huang *et al.* 2001; Krupke *et al.* 2003). It is also shown that (Liu *et al.* 2002; Rao *et al.* 2003; Nuraje *et al.* 2004; Tsukruk *et al.* 2004; Myung *et al.* 2005) the SAM (self-assembled monolayer) patterns can

be utilized to direct the assembly of nanoscale wires such as SWNT (Iijima 1991) onto specific locations of the substrates. The experimental images of Im *et al.* (2006c) suggest that adsorption of these molecules is irreversible to some extent, i.e. in timescales of relaxation time of CNT, $\tau \propto L^3$. This also suggests irreversible adsorption kinetics plays an important role to determine the adsorption patterns.

The adsorption of long molecules can be considered in two stages: (a) Landing from the bulk to attractive surface sites; (b) Relaxation of the internal degree of freedom of a molecule. The first step, the adsorption (landing) of SWNTs onto relatively large polar SAM patterns, can be described by the standard Langmuir isotherm (Karpovich and Blanchard, 1994). In the Langmuir isotherm, the adsorption rate is proportional to the bulk concentration and the number of the vacant sites, and the desorption rate is proportional to the number of adsorbed molecules. As more and more molecules are adsorbed, the number of available adsorption sites becomes smaller, until the equilibrium coverage is reached. In aqueous solution, the attraction between SWNT is estimated to be about $40k_B T/$nm. This means typical micrometer-long CNTs are strongly attractive to each other resulting in heavy aggregation of SWNTs in aqueous solution. In dichlorobenzene solvent, however, SWNTs disperse very well, implying that the attractive forces between CNTs are yet much weaker than that in water. Hence, the progress of SWNT adsorption onto polar SAM favors less and less incoming flux. If we neglect CNT–CNT interaction ($\varepsilon_{CNT} \ll \varepsilon_{ads}$), the equilibrium surface coverage is obtained when $\varepsilon_{ads} + k_B T \ \log(\theta b^2) = k_B T \ \log(Cb^3)$ with θ and C being the surface and bulk concentration of CNTs, respectively, and b is the length unit.

Let us consider a SWNT that is confined in a two-dimensional plane, a so-called "sliding chamber", in order to investigate the relaxation of the internal degree of freedom as shown in Fig. 10.2 (Im *et al.* 2006a).

For a long molecule to adsorb, the initial segments landed with a certain angle with patterned attractive sites adsorb first. Rotational diffusion allows exploring around the fixed strand. If only a fraction of a SWNT falls on the attractive region, the remaining fluctuating part (landed in a non-polar part) diffuses and eventually adsorbs on the polar region, trading off the bending energy cost. This kinetics is similar to Kramer's reaction theory (reaction through the energy barrier).

The rotational and translational mobility of SWNT depends on the surface conditions. The reason for small mobility on polar SAMs is attributed to strong adhesion forces and more importantly "chemical roughness", which often appears in experimental situations and breaks translational invariance. Experimentally, the "sliding" mobility to SWNTs in a sliding chamber is provided by thermal energy or ultrasonic vibration until the SWNTs spread uniformly on the surface. Without sonication, SWNTs start landing. In the chamber, the segments of the SWNTs perform mainly diffusive motions until they are captured by the interaction range of surface binding sites. The aforementioned segments, lying initially on the polar region, are immobile at least on the timescale of interest during which segments on the non-polar region move and accumulate at the polar boundary. If the whole SWNT falls on the non-polar region, it will diffuse until some part of the CNT is captured by the polar region

and aligns along the polar–non-polar boundary. If some fraction of a SWNT enters the interaction ranges of a polar SAM, the segment further moves into the pattern until it reaches the other boundary. This process is deterministic. The parts of a SWNT in the non-polar region diffuse until they encounter the attractive polar region (Fig. 10.20). Subsequent adsorption of the remaining segment results in bending toward the polar region with accumulation of bending energy. The strong CNT–polar SAM interactions entail progressive zipping of CNT segments on the polar–non-polar boundary.

The total energy of a SWNT whose fraction is adsorbed on the polar region consists of the adsorption energy of CNT on the polar substrates and bending energy $E_{elastic}$:

$$E_{tot} = \int_0^{l_p} \gamma_p \, ds + \frac{\kappa}{2} \int_0^L \left(\frac{d^2 r}{ds^2} \right)^2 ds,$$

where $\gamma_p (<0)$ is the interface energy per unit length for the SWNT segments on a polar SAM and $\kappa / k_B T$ is the so-called persistence length that represents the bending stiffness of SWNTs. L, l_p stands for the total SWNT length and the segment length landed on the polar region. The integration is performed following the contour of the SWNT segments. An adsorption experiment (Im *et al.* 2006a) indicates that the attractive energy of SWNT segments on a non-polar SAM or other SWNTs is negligible, and the interface energy terms of those segments are omitted. We also neglect the entropic contribution, which is of the order of $k_B T$. The equilibrium conformation will be obtained by minimizing the free-energy condition. The aggregated CNTs expected to align straight and accumulate in polar SAM regions (Fig. 10.21(b)). We found that the SWNTs are often trapped in local energy-minimum states. In order to escape from local minima, a large activation energy is required. We estimate the energy barrier from the curved conformation of CNT bundles at the polar boundary (Fig. 10.21(a)). The curved structure lasts as long as the accumulated bending energy is smaller than the energy barrier. When the total stored energy exceeds the energy barrier, the overall SWNT shape straightens, as is shown in Fig. 10.21(b). From the measured value of the typical radius of curvature $r \sim 1.34 \, \mu m$ of a micrometer-long SWNT segment, we estimate that the restoring force is about 0.056 pN and the typical energy barrier associated with the roughness for a micrometer-long SWNT is about $13 k_B T$ per $1 \, \mu m$.

10.4 Characteristics of self-assembled hybrid nanodevices

The feature size of silicon-based transistors has been reduced exponentially as Moore's law indicates. Nowadays, current semiconducting industries have, however, confronted a fundamental obstacle preventing further size reduction by top-down approaches. Over the past decade, various research efforts in nanoscience and nanotechnology have shown that nanostructured materials including carbon nanotubes and nanowires can be used as various electronic
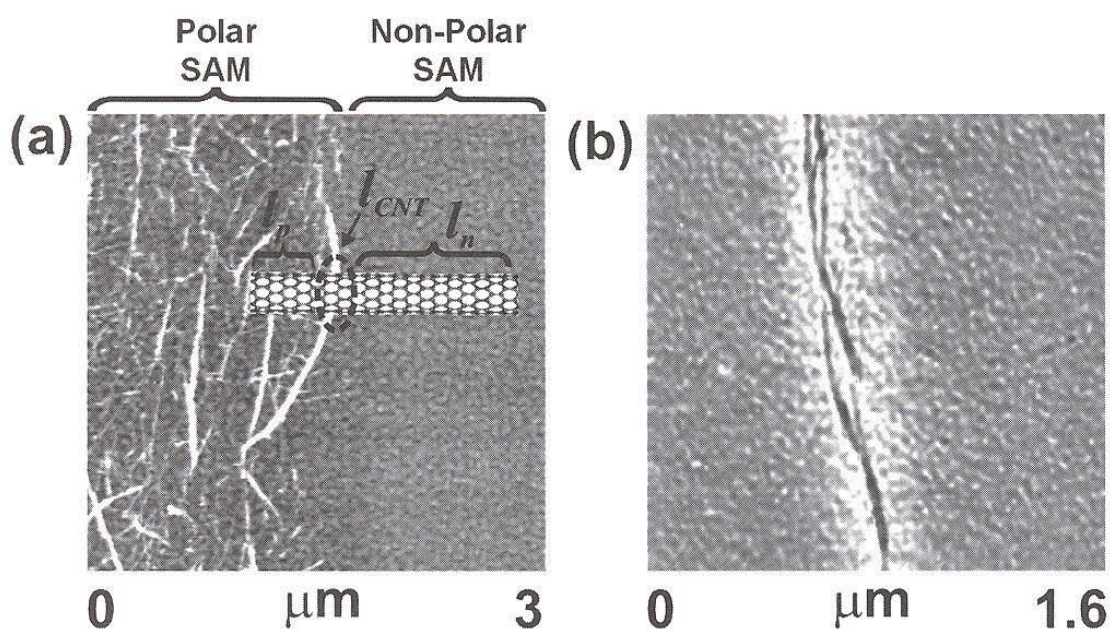
Fig. 10.21 (a) Schematic diagram showing a SWNT assembled on pre-existing SWNT patterns and AFM topography image of SWNTs assembled onto the patterns on polar and non-polar regions. (b) High-resolution lateral force image of SWNTs aligned on polar SAM patterns (from Im, J., Huang, L., Kang, J., Lee, M., Lee, D.J., Rao, S.G., Lee, N.-K. and Hong, S. (2006) *J. Chem. Phys.* **124**, 224707 ©2006 American Institute of Physics, reprinted in part with permission).

devices or device elements. In this section, we will describe device characteristics of a wide range of such new devices from a single carbon-nanotube device to self-assembled network devices.

10.4.1   Electronic and transport properties of carbon nanotubes

Depending on their chirality and diameter, single-wall nanotubes can be either metallic or semiconducting (Hamada *et al.* 1992; Mintmire *et al.* 1992; Saito *et al.* 1992). In this section, we review this unique electronic structure and electrical transport properties of single-wall carbon nanotubes.

The electronic band structure of a nanotube somewhat resembles that of a graphene sheet. The difference between the two cases comes from the periodic boundary conditions. A graphene sheet is regarded as an infinitely extended two-dimensional plane, whereas a nanotube is a one-dimensional structure that is infinitely long along the tube axis. However, the periodic boundary condition, $\mathbf{C} \cdot \mathbf{k} = 2\pi l$, is imposed for a finite period along the circumference. Here, $\mathbf{C}$ is a chiral vector defining the chiral index (n, m) of a nanotube; $\mathbf{k}$ is an allowed wave vector; and l is an integer. This results in Bloch wavefunctions with discretely selected wave vectors, which are shown by the straight lines in Fig. 10.22, in the first Brillouin zone of a graphene sheet. Note that the bonding and antibonding π bands, which are located near the Fermi level, are degenerate at the K point in the Brillouin zone of a graphene sheet, while sp^2 σ bands are located far from the Fermi level. Therefore, if at least one of the selected wave vectors crosses the K point, the nanotube becomes metallic.
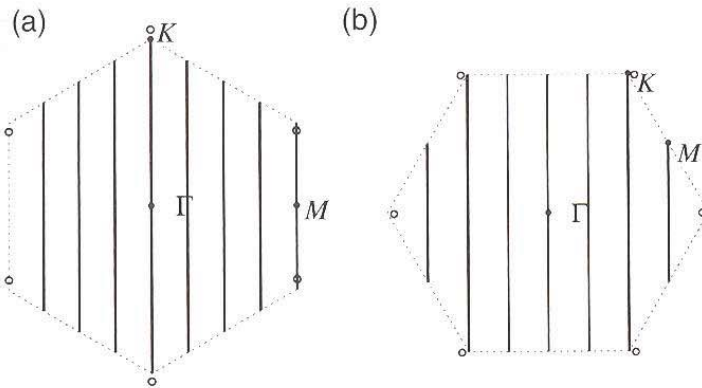
Fig. 10.22 Due to the periodic boundary condition along the circumference, only discrete wave vectors are allowed on the Brillouin zone of a graphene sheet. The allowed wave vectors are, for example, shown in (a) for a (4, 4) armchair nanotube and in (b) for a (6, 0) zigzag nanotube. Open circles show the degenerate point shifted from the K point.

The degenerate point in the nanotube, however, does not exactly correspond to the K point due to its curvature causing p_z atomic orbitals, which point in the radial direction, not to be exactly parallel to each other. Thus, the σ-bond components are incorporated and thus an additional electron transfer is produced between those orbitals. Hence, metallic nanotubes classified in this way become small-bandgap semiconductors with an exception of (n, n) armchair nanotubes, which are truly metallic regardless of their curvature, as discussed below.

Figure 10.22 explains this situation for achiral nanotubes. The vertical lines in Fig. 10.22(a) show the set of allowed wave vectors of a (4, 4) armchair nanotube on the first Brillouin zone of a graphene sheet, which is surrounded by the dashed line in the figure. Although the degenerate point is shifted from the K point to the positions shown by open circles, by the enhancement of the electron transfer along the tube circumference, it is always on the $\Gamma - K$ line, which exactly overlaps with one of the allowed wave vectors. Therefore, the nanotube becomes truly metallic. This feature is essential for any (n, n) armchair nanotubes. The set of allowed wave vectors of a (6, 0) zigzag nanotube is shown in Fig. 10.22(b). Although one of the allowed wave vectors crosses the K point, the shifted degenerate point shown by the open circles is not crossed by any of the allowed wave vectors. Therefore, this tube is not metallic, but narrow-bandgap semiconducting. For general $(n, 0)$ zigzag nanotubes, the allowed wave vectors cross the points that divide the doubled $\Gamma - M$ line into n parts. If n is a multiple of 3, one of the allowed wave vectors crosses the K point, which is close to the degenerate point, like in a (6, 0) nanotube and thus the $(n, 0)$ tube will be a narrow-bandgap semiconductor. If n is not a multiple of 3, then the tube will be a moderate- or wide-bandgap semiconductor.

By using periodic boundary conditions, the condition for general (n, m) nanotubes to be either metallic or semiconducting can be easily derived. The condition is

$$n - m \begin{cases} = 0, & \text{for metallic nanotubes} \\ = 3q, & \text{for narrow-bandgap semiconducting nanotubes} \\ \neq 13q, & \text{for wide-bandgap semiconducting nanotubes,} \end{cases}$$

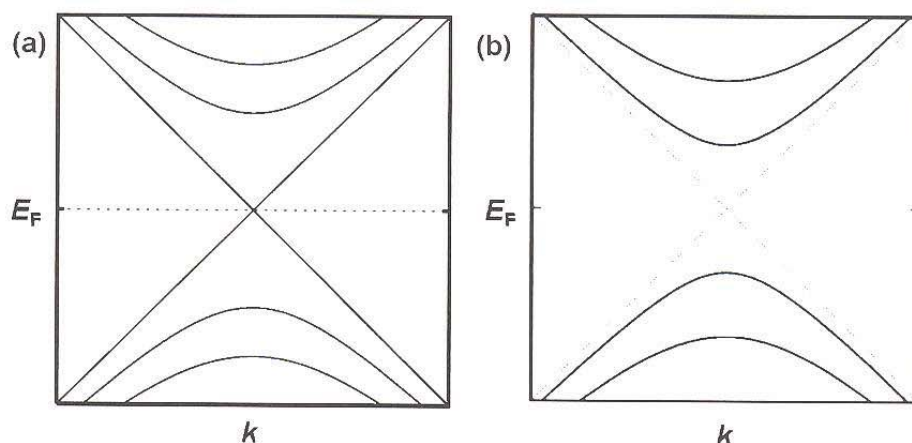where q is any non-zero integer.

Fig. 10.23 Band structures of (a) metallic armchair and (b) semiconducting carbon nanotubes near the Fermi level along the tube axis. These band diagrams were plotted near the K point in the Brillouin zone of graphene.

Electronic band structures of carbon nanotubes near one of the K points of graphene and near the Fermi level are shown in Fig. 10.23, where (a) is for a metallic armchair (n, n) nanotube and (b) is for semiconducting one. The electronic band structure of single-wall (Hamada *et al.* 1992; Mintmire *et al.* 1992; Saito *et al.* 1992) and multiwall carbon nanotubes (Saito *et al.* 1993; Lambin *et al.* 1994; Kwon *et al.* 1998b), as well as single-wall nanotube ropes (Delaney *et al.* 1998; Kwon *et al.* 1998a) is now well documented. It has been shown that interwall coupling leads to the formation of pseudogaps near the Fermi level in multiwall nanotubes (Kwon *et al.* 1998b) and single-wall nanotube ropes (Delaney *et al.* 1998; Kwon *et al.* 1998a), the latter of which were later confirmed by experiments (Ouyang *et al.* 2001). Note that these different electronic structures are determined only by the geometry of the nanotubes depending on how they have been rolled from the planar graphene structure and their relative orientation with respect to neighboring hexagonal configurations. This fact implies that nanotube samples should be a mixture of metallic and semiconducting nanotubes unless they are separated in controlled ways. Experimentally synthesized samples are indeed a mixture of different chiral nanotubes and one of most serious issues in various nanotube research fields.

According to the scattering theory (Landauer 1970), the conductance is expected to be $2G_0$, where $G_0 = 2e^2/h \approx (12.9 \, k\Omega)^{-1}$ is the quantum conductance (Tian and Datta 1994; Lin and Shung 1995; Chico *et al.* 1996). Direct evidence of the delocalization of the wavefunction along the tube axis has been already shown (Bockrath *et al.* 1997; Tans *et al.* 1997), while a direct measurement of the conductance quantization for single-wall nanotubes was recently done (Purewal *et al.* 2007). Electron transport in perfect single nanotubes is believed to be ballistic in nature, implying the absence of inelastic scattering. Conductance measurements of multiwall carbon nanotubes raised a significant controversy due to the observation of unexpected conductance values, in apparent disagreement with theoretical predictions (Frank *et al.* 1998). In these experiments, multiwall carbon nanotubes, when brought into contact with liquid mercury, exhibit not only even, but also odd multiples of the conductance quantum G_0. An even bigger surprise was the observation of
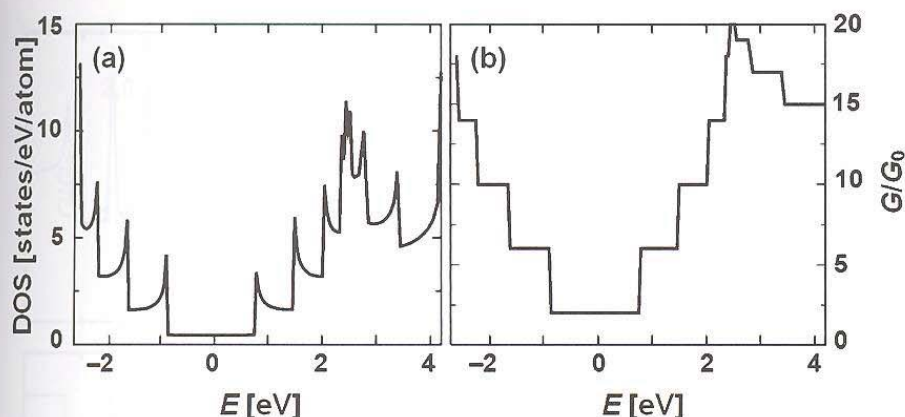
Fig. 10.24 Electronic density of states (DOS) (a) and conductance G (b) of an isolated single-wall (10, 10) carbon nanotube. The DOS is given in arbitrary units, and G is given in units of the conductance quantum $G_0 = 2e^2/h$ (from Sanvito, S., Kwon, Y.-K., Tománek, D. and Lambert, C.J. (2000) *Phys. Rev. Lett.* **84**, 1974 ©2000 The American Physical Society, reprinted in part with permission).

non-integer quantum conductance values, such as $G \approx 0.5\,G_0$, since conductance is believed to be quantized in units of G_0 (Landauer 1970).

The unexpected conductance behavior can arise from the interwall interaction in multiwall or in bundled nanotubes (Sanvito *et al.* 2000). This interaction may not only block some of the quantum conductance channels, but also redistribute the current non-uniformly over the individual tubes. Under the experimental conditions described in Frank *et al.* (1998), this effect may reduce the conductance of the whole system to well below the expected value of G_0.

The scattering technique determines the quantum-mechanical scattering matrix S of a phase-coherent "defective" region that is connected to "ideal" external reservoirs (Sanvito *et al.* 1999). At zero temperature, the energy-dependent electrical conductance $G(E)$ is given by the Landauer–Büttiker formula (Büttiker *et al.* 1985)

$$G(E) = \frac{2e^2}{h} T(E),$$

where $T(E)$ is the total transmission coefficient evaluated at the energy E, which, in the case of small bias, is the Fermi energy E_F.

For a homogeneous system, $T(E)$ assumes integer values corresponding to the total number of open scattering channels at the energy E. For individual (n, n) armchair tubes, this integer is further predicted to be even (Tian and Datta 1994; Lin and Shung 1995; Chico *et al.* 1996), with a conductance $G = 2G_0$ near the Fermi level. As a reference to previous results, the density of states and the calculated conductance of an isolated (10, 10) nanotube is shown in Fig. 10.24.

The corresponding results for the (10, 10)@(15, 15) double-wall nanotube (Kwon *et al.* 1998b) and the (5, 5)@(10, 10)@(15, 15) triple-wall nanotube, where the interwall interaction significantly modifies the electronic states near the Fermi level, are shown in Figs. 10.25. The density of states of the double- and the triple-wall nanotubes are shown in Figs. 10.25(a) and (b), respectively. The corresponding results for the total conductance are given in Figs. 10.25(c) and (d), respectively. The conductance results suggest that some of the conduction channels have been blocked close to E_F. The interwall interaction, which is responsible for this behavior, also leads to a redistribution of the total conduction current over the individual tube walls. The partial conductances of
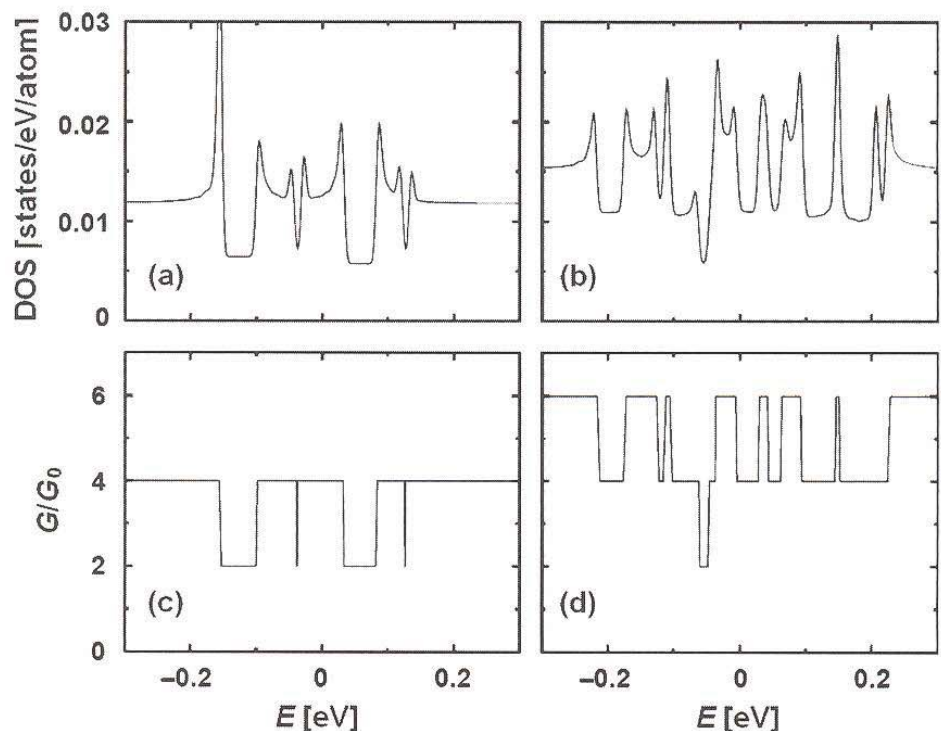
Fig. 10.25 Electronic density of states and conductance of a double-wall (10, 10)@(15, 15) nanotube [(a) and (c), respectively] and a triple-wall (5, 5)@(10, 10)@(15, 15) nanotube [(b) and (d), respectively] (from Sanvito, S., Kwon, Y.-K., Tománek, D. and Lambert, C.J. (2000) *Phys. Rev. Lett.* **84**, 1974 ©2000 The American Physical Society, reprinted in part with permission).

the tube walls are defined accordingly as projections of the total conductance and shown in Fig. 10.26. It is noticed that the partial conductance is strongly non-uniform within the pseudogaps, where the effects of intertube interactions are stronger.

The interwall interaction in multiwall nanotubes not only blocks certain conduction channels, but also redistributes the current non-uniformly across the walls. The interwall interaction will play a similar role in a bundle of single-wall nanotubes, or a rope. Such interwall interaction becomes important when new nanoscale devices are formed from nanotube networks. We will discuss the electrical characteristics of network-based devices in the next section.

10.4.2   Electronic and transport properties of network devices

In this section, we will describe electronic and transport properties of hybrid nanodevices based on mixed-chirality nanotube networks, which are readily available to industry. No theoretical foundation for nanocomposite network thin-film transistors comparable to Shockley's theory of classical transistors currently exists. We have developed a methodology for modelling the electrical properties of nanotube composite thin films, and optimizing the production specifications for yielding the optimal performance, while minimizing the number of defective components. Our computational approach is to model the device as a random dispersion of nanotubes. The dispersion can be modelled with fractal diffusion taking into account the lens effect of the substrate template that imposes alignment of the nanotubes at the channel edges. The dispersion is also represented as a grid of resistors and nodes. Using
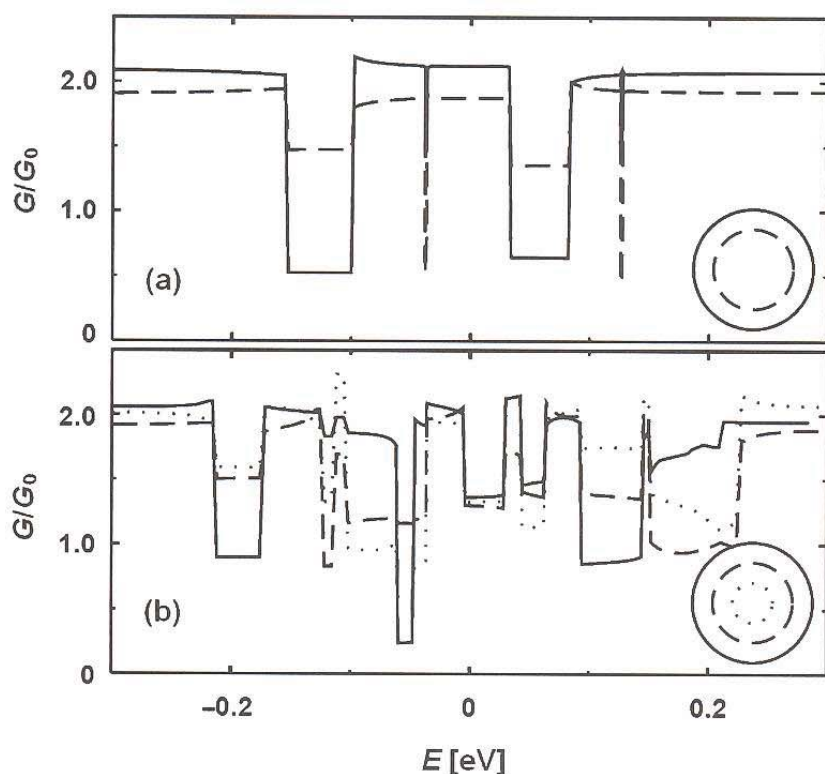
Kirchhoff's laws and measured and modelled nanotube conductance and nanotube junction conductance, the electronic properties of individual model channels can be estimated. A Monte Carlo approach to statistically characterize outcomes shows the optimal channel dimensions and nanotube density resulting in the most semiconducting devices; and models ensemble statistics of the electrical properties of these thin films.

10.4.2.1   *Model description*

Figure 10.27 shows a birds eye view of a mixed-chirality network. We can regard it as a system of percolating sticks. Here, the solid lines represent metallic nanotubes and the dashed lines semiconducting nanotubes. The overlay shows possible subregions that would result from such dispersion on a template. We know from fractal or percolation theories that an infinitely large network of sticks will percolate at a threshold density of $\rho_{Th} = 4.26^2/\pi L_S^2$ or higher. This value is about 0.64 nanotubes in 1 μm^2 for a random dispersion of 3-μm nanotubes. Channels are not infinite in extent, and local regions have three possible connectivity classes as shown in Fig. 10.27. The first possibility is that connectivity is broken, so that the device lacks a conducting path from the one electrode to the other. If all the tubes are semiconducting, high densities would solve this problem. But with mixed chirality, a high density in which the fraction of metallic tubes will result in a device with metallic properties. For the infinite extent channel, when the density of metallic CNTs becomes 0.64 NTs/μm^2, the device will be metallic. The second possible outcome is a channel that has a conducting path from one electrode to the other exclusively with metallic tubes. The broken connectivity and the metallic
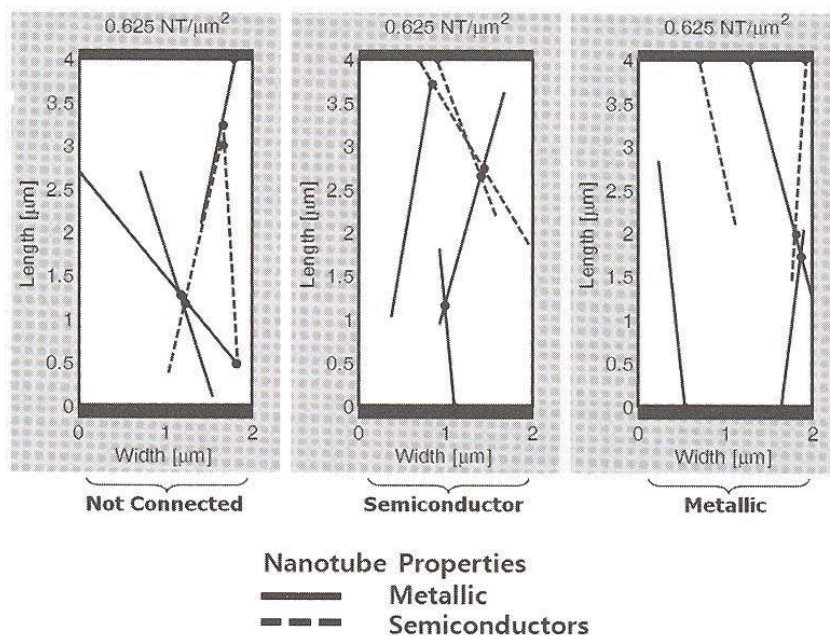
Fig. 10.27 Classification of the different chirality of assembled SWNTs in channels.

connectivity are undesired outcomes. What industry seeks are techniques for creating semiconducting channels of nanotube networks. The third possible outcome is a channel with at least one semiconducting nanotube along each path of nanotubes connecting the two electrodes. Thus, there are three possible classes of devices: not connected, metallic, and semiconducting. Our model can be used to predict the likelihood of each class for a given set of processing parameters.

A conceptual block diagram of our model is provided in Fig. 10.28. The inputs to the model are the channel dimensions, fraction of metallic nanotubes, and nanotube density. These are the parameters used to describe a single channel or a single device. The number of trials for the Monte Carlo statistics is also an input and specifies the number of such devices that will be modelled in the simulation. As the model runs it accesses a database of nanotube properties. The model outputs the probability distribution functions for each class. A bias voltage can be specified to model $I–V_g$ curves for individual channels.

The program is modular and the database is flexible and extensible. Currently, there are nominal properties for nanotube conductivity operating at room temperatures, in an ambient environment, and dispersed on a generic substrate. The program is designed to allow the database to grow and include nanotube properties including alternative algorithms for the dispersion statistics (the position and orientation in the channel) that simulate bundling or other dynamics; and nanotube properties that are environmentally active to address questions of using the thin film as a sensor and modelling the sensor performance or determining when a device might fail; and compare the performance of different chirality mixtures on different substrates.

The central algorithm is shown in Fig. 10.29. First, a channel is modelled by populating it with nanotubes. Internally, the orientation and classification (defining properties) of each nanotube is maintained in a list. Next, the
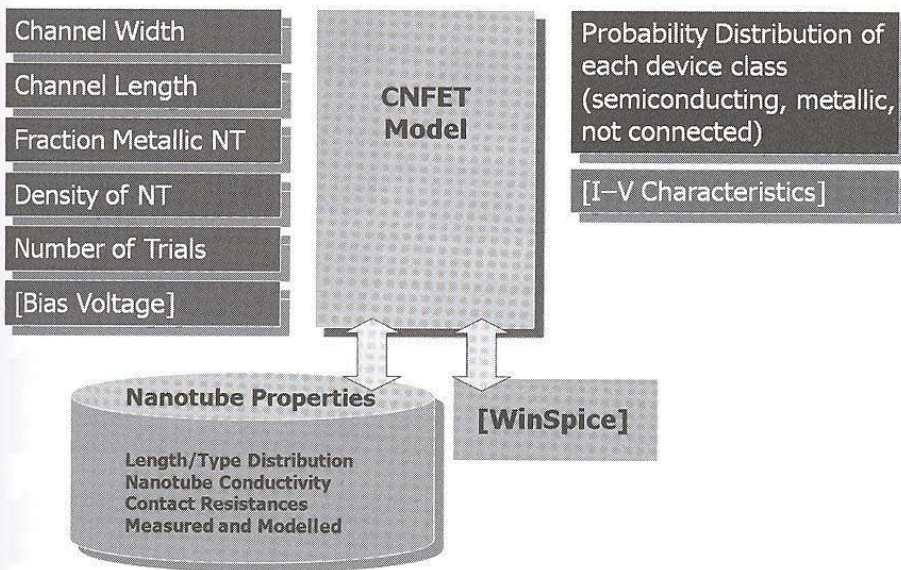
Fig. 10.28 Conceptual block diagram describing our model.

locations where nanotubes contact the electrodes and the nanotube junctions in the channel are found. These locations are used to segment the nanotubes into resistors and nodes. This equivalent circuit is analyzed to determine path connectivity and assign a classification: broken, metallic, or semiconducting, to the device channel. The electronic properties are determined by solving the equivalent circuit using WinSpice. Performing this sequence many times to acquire statistics for the probability distribution functions of each class as a function of density or other manufacturing variable.

10.4.2.2 *Monte carlo results*

The probability distributions as functions of nanotube density are shown in Fig. 10.30. The dashed lines represent the percentage of semiconducting nanotube networks as a function of CNT densities. Manufacturers want a high probability of semiconducting nanotubes, and processing parameters that are not too sensitive to variation. For example, the statistics ideally won't change significantly as the width, length or density changes. Optimally, the high turnout of semiconducting networks will occur for a wide range of densities, not within a narrow peak.

The probability distribution of not-connected networks resembles the Fermi–Dirac distribution function starting with 100% not connecting, having a nearly linearly slope near the 50% not connecting point, and ending with 100% connecting, shown with solid lines in Fig. 10.30. In percolation theory, the percolation threshold characterizes the criteria at which a system will percolate. But this applies generally to systems that are infinite in extent. It is inconvenient to use a percolation threshold to characterize systems of percolating sticks that are directional and finite in extent. A more convenient metric for characterizing connectivity is the reference point at which 50% of the channels percolate. When the channel width is held constant the ρ_0 point occurs at higher densities, as the channel length is increased.

When the channel length is held constant, the ρ_0 point occurs at lower density as the width increases. This result is counterintuitive at first glance, when
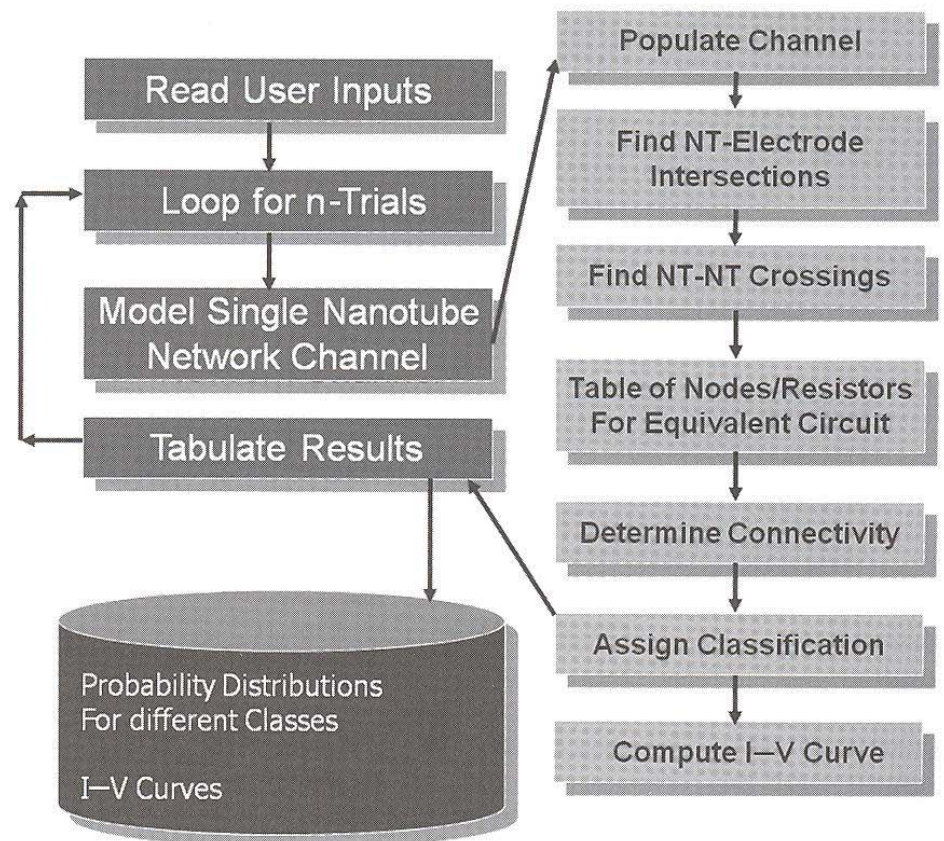
Fig. 10.29 Central algorithm of the model.

considering percolation as a function of area. But the channel connectivity imposes a directional connectivity. Consider two channels side by side. The probability for both being unconnected follows the product rule, thus 75% will have at least one of the two channels connecting at the single channel ρ_0 density point. Thus, doubling the channel width substantially increases the number of connecting devices. The final set in Fig. 10.30 illustrates the sensitivity to small changes in chirality mix. Even a small change in the fraction of metallic content can result in significantly more or fewer metallic devices.

10.4.2.3   *Nanotube network electronic properties*

Our database currently focuses on four resistances for modelling the equivalent circuit. First, measurements of metallic SWNT are length dependent and about $4\,k\Omega/\mu m$ (McEuen and Park 2004). The conductivity of the semiconducting nanotubes is reported to be length dependent and dependent on the gate voltage (Burke 2002; McEuen and Park 2004; Llani *et al.* 2006). Nanotubes have been found to have conductances that vary inversely as length and are proportional to applied voltage (McEuen and Park 2004):

$$G = \mu C_g \left(V_g - V_{g0} \right) / L,$$

where C_g is the capacitance per unit length of the tube, V_{g0} is the threshold voltage, μ is the mobility, and L is the tube length. Here, an array of
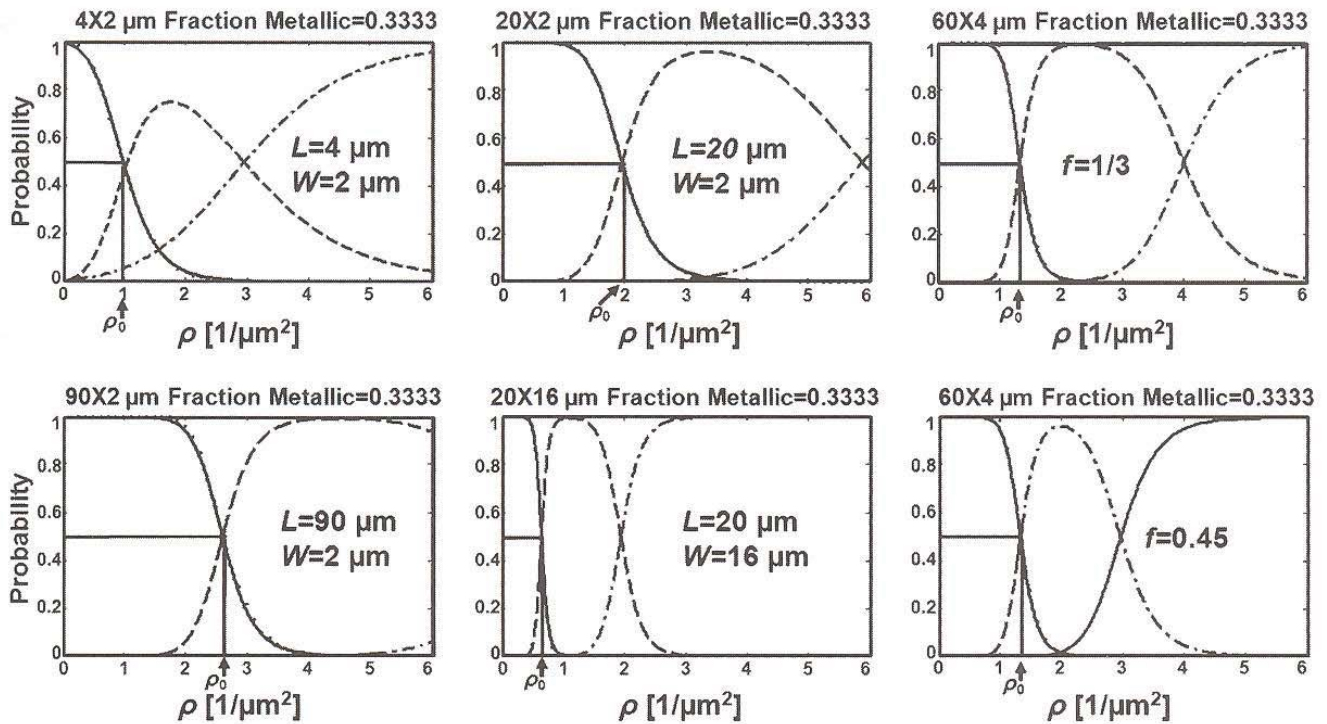
Fig. 10.30 Probability distributions as functions of nanotube density with selected manufacturing parameters. The solid lines represent "not connected" devices; the dashed lines show the probability of semiconducting devices at a given density, whereas the dash-dotted lines do this for metallic devices.

values is generated to create an *I–V* curve, though the factor of capacitance and mobility can vary significantly. Nanotube mobilities have been measured from 1000–10 000 cm^2/V s for CVD tubes, and recently a value as high as 200 000 cm^2/V s has been reported for graphene (Bolotin *et al.* 2008). The electrical measurements were done on various junctions of crossed nanotubes (Fuhrer *et al.* 2000) and modelled computationally (Yoon *et al.* 2001). We used a nominal value of 40 kΩ but these are highly sensitive to pressure, so that the network might be useful as an electromechanical sensor. Finally, we set the contact resistance between a nanotube and an electrode to be 50 kΩ.

The shape of the resulting *I–V* curves resembles those found experimentally as shown in Fig. 10.31. We find similar orders of magnitude difference for semiconducting and metallic networks, but the capacitance/mobility factor could change the outcome significantly.

We have shown that nanotube networks exhibit excellent semiconducting properties; and it is possible to produce hybrid nanodevices from mixed-chirality nanotubes. We have developed a model for estimating the probability of successful and defective semiconductors resulting from a set of manufacturing parameters. For example, over 90% of devices with $40 \times 2 \, \mu m^2$ channel dimension, of 1/3 metallic content, and $\rho = 4$ NTs/μm^2 will have semiconducting properties.
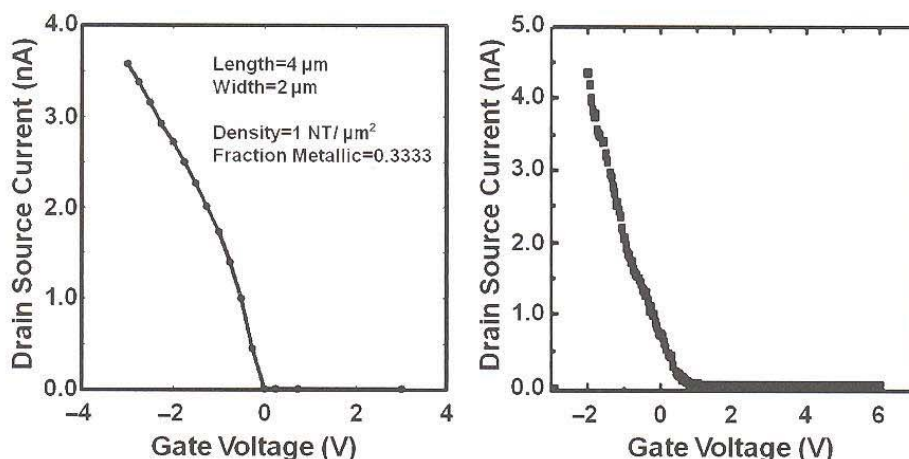
Fig. 10.31 I–V_g characteristic calculated (left) and experimental measured one (right).

10.5 Conclusion

The self-assembly process has been a key strategy in building biological systems for billions of years. This process is now being used to assemble inorganic nanostructures for large-scale functional devices. The self-assembly strategy has been used for various device fabrication methods such as pen-writing, printing, and directed assembly. The advanced fabrication strategy allows us to pattern quite versatile materials such as organic molecules, nanoparticles and nanowires, and it enabled the fabrication of functional devices such as carbon-nanotube network-based transistors. Considering that most new nanostructures are prepared in solution or powder form, the self-assembly strategy is expected to play a key role in nanomanufacuring of hybrid devices based on nanomaterials in the future.

Acknowledgments

References

Adamson, A.W., Gast, A.P. *Physical Chemistry of Surfaces*, 6th edn (John Wiley & Sons Inc., New York, 1997).

Ahn, J., Kim, H., Lee, K.J., Jeon, S., Kang, S.J., Sun, Y., Nuzzo, R.G., Rogers, J.A. *Science* **314**, 1754 (2006).

Baca, A.J., Meitl, M.A., Ko, H.C., Mack, S., Kim, H., Dong, J., Ferreira, P.M., Rogers, J.A. *Adv. Funct. Mater.* **17**, 3051 (2007).

Bernard, A., Renault, J.P., Micheal, B., Bosshard, H.R., Delamarche, E. *Adv. Mater.* **12**, 1067 (2000).

Bockrath, M., Cobden, D.H., McEuen, P.L., Chopra, N.G., Zettl, A., Thess, A., Smalley, R.E. *Science* **275**, 1922 (1997).

Bodas, D., Malek, C.K. *Sens. Actuators B* **123**, 368 (2007).

Bolotin, K.I., Sikes, K.J., Jiang, Z., Klima, M., Gudenberg, G., Hone, J., Kim, P., Stormer, H.L. *Solid State Commun.* **146**, 351 (2008).

Busnaina, A. *Nanomanufacturing Handbook* (CRC Press, Boston, 2007) p. 34–37.

Burke, P.J. *Proc. IEEE-NANO*, **2002**, 393 (2002).

Büttiker, M., Imry, Y., Landauer, R., Pinhas, S. *Phys. Rev. B* **31**, 6207 (1985).

Chaudhury, M.K., Weaver, T. *J. Appl. Phys.* **80**, 30 (1996).

Cherniavskaya, O., Adzic, A., Knutson, C., Gross, B.J., Zang, L., Liu, R., Adams, D.M. *Langmuir* **18**, 7029 (2002).

Chico, L., Benedict, L.X., Louie, S.G., Cohen, M.L. *Phys. Rev. B* **54**, 2600 (1996).

Cho, N., Ryu, S., Kim, B., Schatz, G., Hong, S. *J. Chem. Phys* **124**, 024714 (2006).

Choi, J., Kim, D., Yoo, P.J., Lee, H.H. *Adv. Mater.* **17**, 166 (2005).

Crank, J. *The Mathematics of Diffusion* (Clarendon, Oxford, 1993).

Csucs, G., Michel, R., Lussi, J.W., Textor, M., Danuser, G. *Biomaterials* **24**, 1713 (2003).

Dash, J.G. *Contemp. Phys.* **30**, 2 (1989).

Delamarche, E., Donzel, C., Kamounah, F.S., Wolf, H., Geissler, M., Stutz, R., Winkel, P.S., Michel, B., Mathieu, H.J., Schaumburg, K. *Langmuir* **19**, 8749 (2003).

Delaney, P., Choi, H.J., Ihm, J., Louie, S.G., Cohen, M.L. *Nature* **391**, 466 (1998).

Demers, L.D., Park, S.-J., Taton, T.A., Li, Z., Mirkin, C.A. *Angew. Chem. Int. Ed.* **40**, 3071 (2001).

Donzel, C., Geissler, M., Bernard, A., Wolf, H., Michel, B., Hilborn, J., Delamarche, E. *Adv. Mater.* **13**, 1164 (2001).

Efimenko, K., Wallace, W.E., Genzer, J. *J. Colloid Interf. Sci.* **254**, 306 (2002).

Fan, Z., Ho, J.C., Jacobson, Z.A., Yerushalmi, R., Alley, R.L., Razavi, H., Javey, A. *Nano Lett.* **8**, 20 (2008).

Feng, X., Meitl, M.A., Bowen, A.M., Huang, Y., Nuzzo, R.G., Rogers, J.A. *Langmuir* **23**, 12555 (2007).

Frank, S., Poncharal, P., Wang, Z.L., de Heer, W.A. *Science* **280**, 1744 (1998).

Fu, L., Dravid, V.P., Johnson, D.L. *Appl. Surf. Sci.* **181**, 173 (2001).

Fuhrer, M.S., Nygard, J., Shih, L., Forero, M., Yoon, Y.-G., Mazzoni, M.S.C., Choi, H.J., Ihm, J., Louie, S.G., Zettl, A., McEuen, P.L. *Science* **288**, 494 (2000).

Furuberg, L., Feder, J., Aharony, A., Jossang, T. *Phys. Rev. Lett.* **61**, 2117 (1988).

Ginger, D.S., Zhang, H., Mirkin, C.A. *Angew. Chem. Int. Ed.* **43**, 30 (2004).

Hamada, N., Sawada, S., Oshiyama, A. *Phys. Rev. Lett.* **68**, 1579 (1992).

Hong, S., Mirkin, C.A. *Science* **288**, 1808 (2000).

Hong, S., Myung, S. *Nature Nanotech.* **2**, 207 (2007).

Hong, S., Kim, T.H., Lee, J., Byun, K., Koh, J., Kim, T., Myung, S. *NANO* **2**, 333 (2008).

Huang, Y., Duan, X., Wei, Q., Lieber, C.M. *Science* **291**, 630 (2001).

Hu, L., Gruner, G. *J. Appl. Phys.* **101**, 016102 (2007).

Hur, S., Khang, D. *Appl. Phys. Lett.* **85**, 5732 (2004).

Hur, S., Kocabas. C., Gaur, A., Park, O.Ok., Shim, M., Rogers, J.A. *J. Appl. Phys.* **98**, 114302 (2005).

Iijima, S. *Nature* **354**, 56 (1991).

Im, J., Huang, L., Kang, J., Lee, M., Rao, S.G., Lee, N.-K., Hong, S. *Nanotechnology* **124**, 224707 (2006a).

Im, J., Kang, J., Lee, M., Kim, B., Hong, S. *J. Phys. Chem. B* **110**, 12839 (2006b).

Im, J., Lee, M., Myung, S., Huang, L., Rao, S.G., Lee, D.J., Koh, J., Hong, S. *Nanotechnology* **17**, 3569 (2006c).

Ivanisevic, A., Mirkin, C.A. *J. Am. Chem. Soc.* **123**, 7887 (2001).

Jaeger, R.C. *Introduction to Microelectronic Fabrication*, 2nd edn., vol. V, Chap. 2 (Prentice Hall, New Jersey, 2002).

Jang, J., Hong, S., Schatz, G.C., Ratner, M.A. *J. Chem. Phys.* **115**, 2721 (2001).

Javey, A., Nam, S., Friedman, R.S., Yan, H., Lieber, C.M. *Nano Lett.* **7**, 773 (2007).

Ju, S., Facchetti, A., Xuan, Y., Liu, J., Ishikawa, F., Ye, P., Zhou, C., Marks, T.J., Janes, D.B. *Nature Nanotech.* **2**, 378 (2007).

Kang, J., Myung, S., Kim, B., Oh, D., Kim, G.T., Hong, S. *Nanotechnology* **19**, 095303 (2008).

Kang, S.J., Kocabas, C., Kim, H., Cao, Q., Meitl, M.A., Khang, D., Rogers, J.A. *Nano. Lett.* **7**, 3343 (2007a).

Kang, S.J., Kocabas, C., Ozel, T., Shim, M., Pimparkar, N., Alam, M.A., Rotkin, S.V., Rogers, J.A. *Nature Nanotech.* **2**, 230 (2007b).

Karpovich, D.S., Blanchard, G.J. *Langmuir* **10**, 3315 (1994).

Kim, F., Kwan, S., Akana, J., Yang, P. *J. Am. Chem. Soc.* **123**, 4360 (2001).

Kim, Y., Park, S.J., Koo, J.P., Oh, D.J., Kim, G.T., Hong, S., Ha, J.S. *Nanotechnology* **17**, 1375 (2006).

Kim, Y., Park, S.J., Koo, J.P., Kim, G.T., Hong, S., Ha, J.S. *Nanotechnology* **18**, 015304 (2007).

Kraus, T., Malaquin, L., Schmid, H., Riess, W., Spencer, N.D., Wolf, H. *Nature Nanotech.* **2**, 570 (2007).

Krupke, R., Hennrich, F., von Lohneysen, H., Kappes, M.M. *Science* **301**, 344 (2003).

Kumar, A., Whitesides, G.M. *Appl. Phys. Lett.* **63**, 2002 (1993).

Kumar, A., Biebuyck, H.A., Whitesides. G.M. *Langmuir* **10**, 1498 (1994a).

Kumar, A., Whitesides, G.M. *Science* **263**, 60 (1994b).

Kwon, Y.-K., Saito, S., Tománek, D. *Phys. Rev. B* **58**, R16001 (1998a).

Kwon, Y.-K., Tománek, D. *Phys. Rev. B* **58**, R13314 (1998b).

Lambin, Ph., Philippe, L., Charlier, J.C., Michenaud, J.P. *Comput. Mater. Sci.* **2**, 350 (1994).

Landauer, R. *Philos. Mag.* **21**, 863 (1970).

Lee, K.J., Motala, M.J., Meitl, M.A., Childs, W.R., Menard, E., Shim, A.K., Rogers, J.A., Nuzzo, R.G. *Adv. Mater.* **17**, 2332 (2005).

Lee, K.J., Meitl, M.A., Ahn, J., Rogers, J.A., Nuzzo, R.G. *J. Appl. Phys.* **100**, 124507 (2006a).

Lee, M., Im, J., Lee, B.Y., Myung, S., Kang, J., Huang, L., Kwon, Y.K., Hong, S. *Nature Nanotech.* **1**, 66 (2006b).

Lee, N.-K., Hong, S. *J. Chem. Phys.* **124**, 114711 (2006).

Lee, T., Mitrofanov, O., Hsu, J.W.P. *Adv. Funct. Mater.* **15**, 1683 (2005).

Li, Y., Qian, F., Xiang, J., Lieber, C.M. *Mater. Today* **9**, 18 (2006).

Lim, J.H., Mirkin, C.A. *Adv. Mater.* **14**, 1474 (2002).

Lin, M.F., Shung, K.W.-K. *Phys. Rev. B* **51**, 7592 (1995).

Liu, X., Fu, L., Hong, S., Dravid, V.P., Mirkin, C.A. *Adv. Mater.* **14**, 231 (2002).

Llani, S., Donev, L.A.K., Kindermann, M., McEuen, P.L. *Nature Phys.* **2**, 687 (2006).

Love, J.C., Estroff, L.A., Kriebel, J.K., Nuzzo, R.G., Whitesides, G.M. *Chem. Rev.* **105**, 1103 (2005).

Manandhar, P., Jang, J., Schatz, G.C., Ratner, M.A., Hong, S. *Phys. Rev. Lett.* **90**, 115505 (2003).

McEuen, P.L., Park, J.-Y. *MRS Bull.* **29**, 272 (2004).

Meitl, M.A., Zhou, Y., Gaur, A., Jeon, S., Usrey, M.L., Strano, M.S., Rogers, J.A. *Nano Lett.* **4**, 1643 (2004).

Meitl, M.A., Zhu, Z., Kumar, V., Lee, K.J., Feng, X., Huang, Y., Adesida, I., Nuzzo, R.G., Rogers, J.A. *Nature Mater.* **5**, 33 (2006).

Menard, E., Lee, K.J., Khang, D., Nuzzo, R.G., Rogers, J.A. *Appl. Phys. Lett.* **84**, 5398 (2004).

Menard, E., Meitl, M.A., Sun, Y., Park, J., Shir, D.J., Nam, Y., Jeon, S., Rogers, J.A. *Chem. Rev.* **107**, 1117 (2007).

Messer, B., Song, J.H., Yang, P. *J. Am. Chem. Soc.* **122**, 10232 (2000).

Miller, S.M., Troian, S.M. *J. Vac. Sci. Technol. B* **20**(6), 2320 (2002).

Mintmire, J.W., Dunlap, B.I., White, C.T. *Phys. Rev. Lett.* **68**, 631 (1992).

Myung, S., Lee, M., Kim, G.T., Ha, J.S., Hong, S. *Adv. Mater.* **17**, 2361 (2005).

Nuraje, N., Banerjee, I.A., MacCuspie, R.I., Yu, L., Matsui, H. *J. Am. Chem. Soc.* **126**, 8088 (2004).

Ouyang, M., Yuan, C., Muisener, R.J., Boulares, A., Koberstein, J.T. *Chem. Mater.* **12**, 1591 (2000).

Ouyang, M., Huang, J.-L., Cheung, C.L., Lieber, C.M. *Science* **292**, 702 (2001).

Park, J., Meitl, M.A., Hur, S., Usery, M.L., Strano, M.S., Kenis, P.J.A., Rogers, J.A. *Angew. Chem. Int. Ed.* **45**, 581 (2006a).

Park, J., Shin, G., Ha, J.S. *Nanotechnology* **18**, 405301 (2007).

Park, S.Y., Kwon, T., Lee, H.H. *Adv. Mater.* **18**, 1861 (2006b).

Pashley, R.M. *J. Colloid. Interf. Sci.* **83**, 531 (1981).

Peterson, E.J., Weeks, B.L., De Yoreo, J.J., Schwarz, P.V. *J. Phys. Chem. B* **108**, 15206 (2004).

Pimparkar, N., Kocabas, C., Kang, S.J., Rogers, J., Alam, M.A. *IEEE Electron Dev. Lett.* **28**, 593 (2007).

Piner, R., Zhu, J., Xu, F., Hong, S., Mirkin. C.A. *Science* **283**, 661 (1999).

Purewal, M.S., Hong, B.H., Ravi, A., Chandra, B., Hone, J., Kim, P. *Phys. Rev. Lett.* **98**, 186808 (2007).

Rao, S.G., Huang, L., Setyawan, W., Hong, S. *Nature* **425**, 36 (2003).

Rozhok, S., Piner, R., Mirkin, C.A. *J. Phys. Chem. B* **107**, 751 (2003).

Saito, R., Fujita, M., Dresselhaus, G., Dresselhaus, M.S. *Appl. Phys. Lett.* **60**, 2204 (1992).

Saito, R., Dresselhaus, G., Dresselhaus, M.S. *J. Appl. Phys.* **73**, 494 (1993).

Santhanam, V., Anders, R.P. *Nano Lett.* **4**, 41 (2004).

Sanvito, S., Lambert, C.J., Jefferson, J.H., Bratkovsky, A.M. *Phys. Rev. B* **59**, 11936 (1999).

Sanvito, S., Kwon, Y.-K., Tománek, D., Lambert, C.J. *Phys. Rev. Lett.* **84**, 1974 (2000).

Schmid, H., Michel, B. *Macromolecules* **33**, 3042 (2000).

Sheehan, P.E., Whitman, L.J. *Phys. Rev. Lett.* **88**, 156104 (2002).

Smith, R.K., Lewis, P.A., Wiess, P.S. *Progr. Surf. Sci.* **75** (2004).

Sun, Y., Rogers, J.A. *Nano Lett.* **4**, 1953 (2004).

Sun, Y., Khang, D., Hua, F., Hurley, K., Nuzzo, R.G., Rogers, J.A. *Adv. Funct. Mater.* **15**, 30 (2005).

Sun, Y., Rogers, J.A. *Adv. Mater.* **19**, 1897 (2007).

Tan, J.L., Tien, J., Chen, C.S. *Langmuir* **18**, 519 (2002).

Tans, S.J., Devoret, M.H., Dai, H., Thess, A., Smalley, R.E., Geerligs, L.J., Dekker, C. *Nature* **386**, 474 (1997).

Tao, A., Kim, F., Hess, C., Goldberger, J., He, R., Sun, Y., Xia, Y., Yang, P. *Nano Lett.* **3**, 1229 (2003).

Tian, W., Datta, S. *Phys. Rev. B* **49**, 5097 (1994).

Trimbach, D.C., Stapert, H., Orselen, J.V., Jandt, K.D., Bastiaansen, C.W.M., Broer, D.J. *Adv. Eng. Mater.* **9**, 1123 (2007).

Tsukruk, V.V., Ko, H., Peleshanko, S. *Phys. Rev. Lett.* **92**, 065502 (2004).

Wang, Z., Zhang, J., Xing, R., Yuan, J., Yan, D., Han, Y. *J. Am. Chem. Soc.* **125**, 15278 (2003).

Wang, Z. L., Lieber, C.M. *MRS Bull.* **32**, 99 (2007).

Weeks, B.L., Noy, A., Miller, A.E., De Yoreo, J.J. *Phys. Rev. Lett.* **88**, 255505 (2002).

Weibel, D.B., Lee, A., Mayer, M., Brady, S.F., Bruzewicz, D., Yang, J., DiLuzio, W.R., Clardy, J., Whitesides, G.M. *Langmuir* **21**, 6436 (2005).

Whang, D., Jin, S., Wu, Y., Lieber, C.M. *Nano Lett.* **3**, 1255 (2003).

Wilkinson, D., Willemsen, J.F. *J. Phys. A* **16**, 3365 (1983).

Wilson, D.L., Martin, R., Hong, S., Cronin-Golomb, M., Mirkin, C.A., Kaplan, D.L. *Proc. Natl. Acad. Sci.* **98**, 13660 (2001).

Xia, Y., Zhao, X.M., Whitesides, G.M. *Microelectron. Eng.* **32**, 255 (1996).

Xia, Y., Whitesides, G.M. *Angew. Chem. Int. Ed.* **37**, 550 (1998).

Yamaki, T., Asai, K. *Langmuir* **17**, 2564 (2001).

Yip, H., Zou, J., Ma, H., Tian, Y., Tucker, N.M., Jen, A.K. *J. Am. Chem. Soc.* **128**, 13042 (2006).

Yoo, P.J., Choi, S., Kim, J.H., Suh, D., Baek, S.J., Kim, T.W., Lee, H.H. *Chem. Mater.* **16**, 5000 (2004).

Yoon, Y.-G., Mazzoni, M.S.C., Choi, H.J., Ihm, J., Louie, S.G. *Phys. Rev. Lett.* **86**, 688 (2001).

Yu, G., Cao, A., Lieber, C.M. *Nature Nanotech.* **2**, 372 (2007).

Zhou, Y., Hu, L., Grüner, G. *Appl. Phys.* **88**, 123109 (2006).